REVIEW

Inkjet-Printed Organic Solar Cells and Perovskite Solar Cells: Progress, Challenges, and Prospect

Xing-Ze Chen[a,b], Qun Luo[a,b*], and Chang-Qi Ma[a,b*]

[a] *School of Nano-Tech and Nano-Bionics, University of Science and Technology of China, Hefei 230027, China*
[b] *i-Lab & Printable Electronics Research Center, Suzhou Institute of Nano-Tech and Nano-Bionics, Chinese Academy of Sciences, Suzhou 215123, China*

Abstract In recent years, the power conversion efficiency of organic solar cells (OSCs) and perovskite (PVSCs) has increased to over 19% and 25%, respectively. Meanwhile, the long-term stability of OSCs and PVSCs was also significantly improved with a better understanding of the degradation mechanism and the improvement of materials, morphology, and interface stability. As both the efficiency and lifetime of solar cells are approaching the commercialization limit, fabrication methods for large-area OSCs and PVSCs that can be directly transferred from lab to fab become essential to promote the industrialization of OSCs and PVSCs. Compared with the coating methods, inkjet printing is a mature industrial technology with the advantages of random digital patterning, excellent precision and fast printing speed, which is considered to have great potential in solar cell fabrication. Many efforts have been devoted to developing inkjet-printed OSCs and PVSCs, and much progress has been achieved in the last few years. In this review, we first introduced the working principle of inkjet printing, the rheology requirements of inks, and the behaviors of the droplets. We then summarized the recent research progresses of the inkjet-printed OSCs and PVSCs to facilitate knowledge transfer between the two technologies. In the end, we gave a perspective on inkjet-printed OSCs and PVSCs.

Keywords Organic solar cells; Perovskite solar cells; Inkjet printing; Ink formulation; Morphology control

1 INTRODUCTION

Organic solar cells (OSCs) have recently attracted much attention as an efficient and sustainable energy technology because of their mechanical flexibility, lightweight, ease of mass manufacturing, and potentially low cost.[1–4] By mixing magnesium phthalide and tetramethyl-*p*-phenylenediamine between different electrodes, Kearns and Calvin[5] realized an organic photovoltaic device with a maximum output power of 3×10^{-12} W, proving the first concept of OSCs. Tang[6] developed heterojunction OSCs based on thermal evaporated organic thin films in 1986 and increased the charge generation rate by reducing the exciton diffusion distance. A power conversion efficiency (PCE) of 1% was achieved. In 1995, Hegger *et al.*[7] proposed the concept of bulk heterojunction structure, where the fullerene electron acceptor ($PC_{61}BM$) and poly-phenylenevinylene donor (PPV) were mixed to form an interpenetrating network. Such a nanoscale donor-acceptor (D-A) network effectively improved the excitons dissociation and charge separation efficiency, and a PCE of 2.9% was achieved. Since then, many efforts have been devoted to developing new organic semiconductors. Nowadays, the power conversion efficiency of OSCs has increased to higher than 19% for the on-fullerene acceptor-based devices.[8,9]

Perovskite solar cells (PVSCs) are the most promising types of solar cells developed in recent year. Since the first report by

Miyasake *et al.*[10] in 2009, the PVSCs sprung to the forefront of photovoltaic research and have been demonstrated to be promising candidates for next-generation solar cells. In 2012, Park and Grätzel *et al.*[11] reported on solid-state mesoscopic heterojunction solar cells with an efficiency of 9.7%, employing $CH_3NH_3PbI_3$ as light harvesters and *spiro*-MeOTAD as a hole transport layer. In 2019, You *et al.*[12] used organic halide salt phenethylammonium (PEAI) to passivate the perovskite surface, and obtained a certified efficiency of 23.32%. Now, tremendous progress has been achieved in the field of perovskite solar cells (PVSCs) in the recent ten years and the highest performance has reached higher than 25%.[13,14] The PVSCs have a similar device structure as the OSCs and could be fabricated through the solution-processable large-area deposition.

These high-performance OSCs and PVSCs were mainly fabricated by spin coating with an area of <0.1 cm². Spin-coating is an effective method to deposit nano-thin films with excellent uniformity. This technique is widely subjected to fundamental studies. However, the scope of spin-coating is extremely limited on the laboratory scale, while unsuitable for upscaling and further industrial applications. The first reason for this is that most of the materials are wasted during spin-coating, yielding a low material utilization. Secondly, spin coating is incompatible with structure patterning, which is essential for solar module fabrication. Thirdly, it is challenging to achieve large-area homogenous film through spin-coating. Therefore, it is urgently needed to develop methods to fabricate large-area OSCs and PVSCs that can be easily transferred from lab to fab. Generally, solution-based thin film deposition methods could be divided into two categories, *i.e.*, coating and printing. The former method includes doctor-blade coating, slot-die coating, and spray coating, and the latter includes gravure printing, screen printing, and inkjet printing. The coating method is usually used to prepare large-area thin films without a pattern, while gravure and screen-printing methods can print patterned thin films using a pre-patterned gravure roller and screen. On the other hand, inkjet printing has high design freedom and can fabricate patterns through digital control. Inkjet printing has been applied to print posters, labels, and packages. Recently, inkjet printing is also used in the preparation of electronic devices, such as organic

light-emitting diode (OLED), organic and perovskite solar cells.

Seeing the great potential of inkjet printing in large-area thin-film fabrication, many efforts have been made in inkjet printing processing for OSCs and PVSCs. Some fundamental questions for inkjet printing OSCs and PVSCs were well studied, such as rheology requirements for the inks, coffee ring issues, droplet formation, coalescence processes, *etc*. Inkjet printing has been used to prepare different functional layers in OSCs and PVSCs, including the bottom and top electrodes, the interfacial layers, and the photoactive layers. Based on these efforts, the highest efficiency of OSCs and PVSCs prepared by inkjet printing has reached 13%[15] and 21.6%, revealing the possibility of high-performance PVSCs through inkjet printing.[16] In this review, we will briefly introduce the working mechanism of inkjet printing, the rheology requirements of inks, and the movement behaviors of the droplets. Then, we will summarize the research progress of inkjet-printed electrodes, the interfacial layers and the photoactive layers of the OSCs and the PVSCs. Besides, the development of fully inkjet-printed cells was introduced and discussed. Finally, the challenges and prospects of OSCs and PVSCs prepared by inkjet printing are presented.

2 GENERAL INTRODUCTION OF INKJET PRINTING

2.1 Working Principle of Inkjet Printing

Inkjet printing is a maskless and contact-free technique that precisely controls the deposition of micrometer-scale ink droplets by ejecting the droplets from the ink cartridge. Inkjet printing offers a high resolution of 1000 drops per inch (corresponding to a drop spacing of 25 μm). Such a deposition process can be easily transferred from lab to fab by simply enlarging the printer. Therefore, inkjet printing technology has been applied in various fields, including display printing,[17] solar cells printing,[18] sensor printing,[19] and drug substances printing.[20]

Depending on the droplets control mechanism, inkjet printing can be divided into two catalogs, continuous inkjet printing (CIP) and drop-on-demand (DOD) inkjet printing. Fig. 1 shows the schematic diagram of CIP and DOD inkjet printing. CIP is the ejection of a nonstop ink flow through a
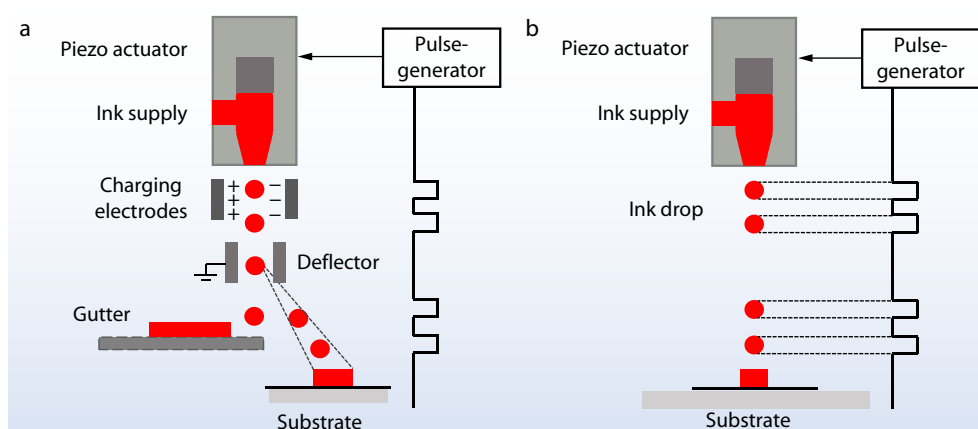

Fig. 1　Schematic of (a) continuous inkjet-printing (CIP) and (b) drop-on-demand (DOD) printing.

nozzle under the surface tension forces. The CIP printing involves three steps: (1) ink flow passes through the nozzle cavity under the action of the piezoelectric transducer, (2) droplets are charged through the charging electrodes, (3) droplets are deflected by an electric pulse field of the defector, and finally printed on the substrate. The frequency of the voltage sensor mainly controls the separation of droplets in the inkjet head. CIP has no physical contact or critical spacing between the nozzle and substrate, allowing printing on rough, curved, and pressure-sensitive surfaces. Because of these advantages, CIP is compatible with flexible and conductive materials and has been applied in high-speed graphical applications, industrial labeling, and engraving of individual data.[21–23]

For DOD inkjet printing, ink droplets are ejected by an acoustic pulse from a repository through an orifice. The ink is extruded from a nozzle by the pressure pulse generated due to the contraction of the chamber. The ink droplets are then formed and printed directly onto the substrate. The pressure pulse mainly comes from the mechanical deformation of the piezoelectric ceramics or the swelling and cracking of the bubbles, which is named as piezoelectric inkjet and thermal bubble inkjet, respectively. DOD inkjet printing has the advantage of higher accuracy relative to CIP printing and can produce a single ink droplet according to specific conditions. DOD inkjet has a broader prospect in practical applications. Currently, the fabrication of OSCs mainly adopts the DOD inkjet printing method. We summarized the inkjet printing machine in literature, most of the inkjet printing machines used in the laboratory are dimatix materials printer (DMP) series machines with a 10 pL printing head produced by Fujifilm corporation, such as DMP 2800, 2831 and 2850. Some industrial printing machines, like KM512LN are also used to fabricate large-area films.

Depending on the ink droplet ejection principles, inkjet printing can be divided into piezoelectric and thermal bubble inkjet technologies.[24] In the piezoelectric inkjet printing process, droplets are ejected through the orifice by the pressure formed by the deformation of the piezoelectric ceramics. Specifically, the small piezoelectric ceramics near the nozzle are deformed under the action of voltage and then squeeze the droplet out of the nozzle. In contrast, in the thermal bubble inkjet printing process, ink droplets are ejected through the orifice with the pressure, which is originated from the bubbling of the solution by heating the ink solution rapidly.

2.2 Properties of Inks for Inkjet Printing

The ink for inkjet printing should satisfy several basic rheological requirements to ensure droplet formation and ejection. Therefore, the viscosity, density, and surface tension of the ink play a significant role in inkjet printing. Fromm developed the dimensionless number Z to evaluate the printability of the inks.[25] The Z number is calculated by the inverse of Ohnesorge number (Oh) according to Eq. (3), where the Reynolds number (N_{Re}) and Weber number (N_{We}) are included (Eqs. 1 and 2):[21,22,26]

$$N_{Re} = \frac{\rho \upsilon \iota}{\eta} \tag{1}$$

$$N_{We} = \frac{\upsilon^2 \rho \iota}{\gamma} \tag{2}$$

$$Z^{-1} = \mathrm{Oh} = \frac{\sqrt{N_{We}}}{N_{Re}} = \frac{\eta}{\sqrt{\gamma \rho \iota}} \tag{3}$$

where η is the viscosity of the ink, ρ is the density, υ is the flow rate, γ is the surface tension, and ι is the characteristic length. Reis and Derby[27] demonstrated that a Z value of 1–10 is appropriate for DOD inkjet printing. When the Z value is lower than 1, it is difficult for the droplets to eject due to the high ink viscosity. On the other hand, many satellites form during printing when the Z value is higher than 10. Fig. 2 shows the suitable physical parameters window for the inkjet-printed ink. Although a Z number of 1–10 is generally considered suitable for inkjet printing, the practical Z number might vary for different inks. Additionally, the flow rate of inks also plays an essential role in ink separating at the nozzle.[28]

2.3 Droplet Ejection

Droplet ejection is the first step during inkjet printing. A stable droplet ejection can only be formed when critical rheological requirements are met. At the stage of droplet ejection, two common phenomenons, satellite drops and nozzle clogging, might occur. When the driving voltage is too high or the ink surface tension is too low, long-tailing ink droplets will form during the falling process, breaking down into small fractions and forming satellite droplets (Fig. 3a). On the other hand, the nozzle clogging is mainly due to the nonhomogeneous distribution of solute particles and fast solvent drying at the nozzle (Fig. 3b). As shown in Fig. 3(c), a good droplet ejection
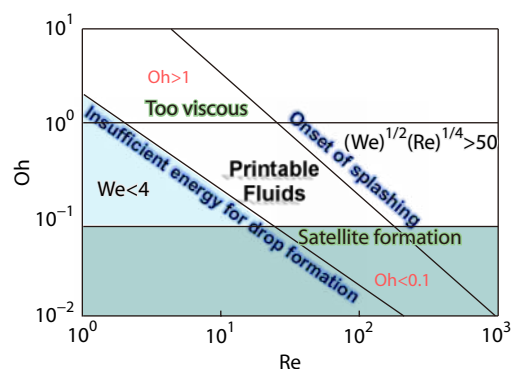

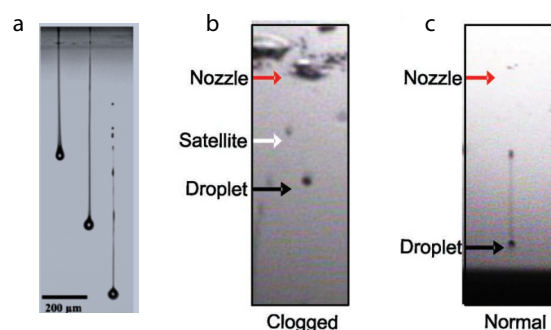**Fig. 2** Empirical physical parameters window for inkjet printable inks.

Fig. 3 Schematic figures of the droplets with (a) satellite drops (Reproduced with permission from Ref. [29]; Copyright (2019) The Royal Society of Chemistry), (b) nozzle clogging, and (c) good droplets ejection. (Reproduced with permission from Ref. [30]; Copyright (2019) Wiley).
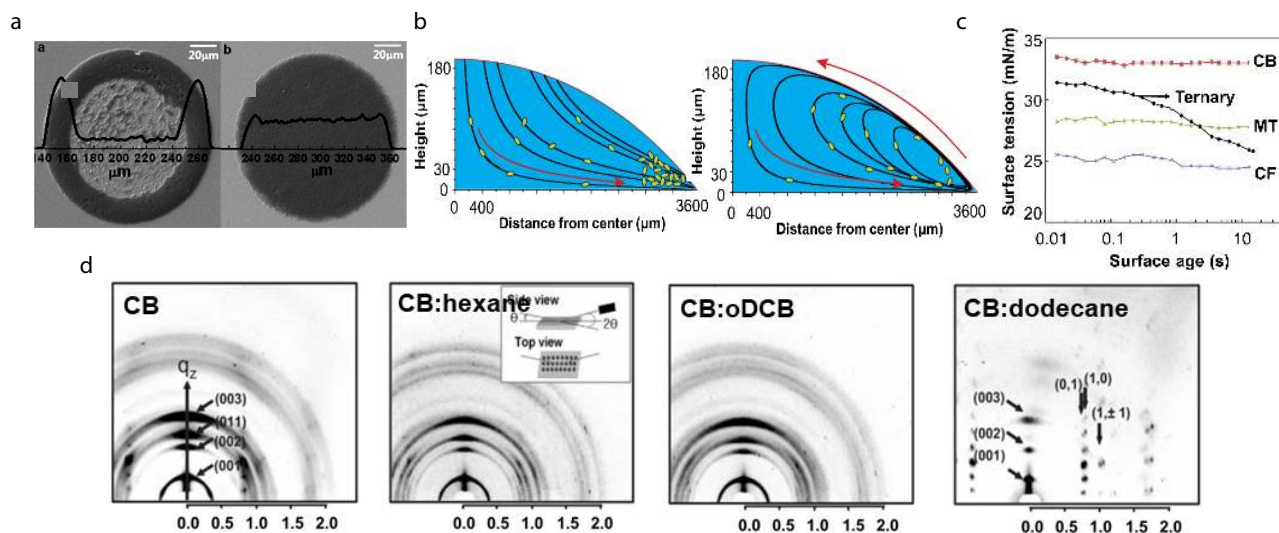
Fig. 4　(a) The photographs of the droplets with and w/o a coffee ring. (Reproduced with permission from Ref. [39]; Copyright (2013) The Royal Society of Chemistry). (b) The Marangoni flow induced by the addition of surfactant overcomes the coffee ring effect. (Reproduced with permission from Ref. [40]; Copyright (2013) Wiley-VCH). (c) The dynamic surface tension of different solvents. (Reproduced with permission from Ref. [37]; Copyright (2014) Wiley-VCH). (d) 2D grazing-incidence X-ray diffraction (2D-GIXD) patterns for TIPS-PEN inkjet-printed from different inks. (Reproduced with permission from Ref. [38]; Copyright (2008) Wiley-VCH).

showed separated droplets without satellites.

2.4 Droplet Drying and the Coffee Ring Effect

During the drying of the droplets, the unbalanced evaporation rates of the solvent and the pining of the edge usually lead to an inhomogeneous solid film, known as the coffee ring effect. Fig. 4(a) shows the drying process of a droplet, where the capillary flow driven by the faster solvent evaporation rate at the edge than in the center brings the solute to the edge. When the Marangoni flow caused by the unbalanced surface tension of the droplet is slower than the capillary flow, solute accumulation at the edge occurs, yielding a much thicker thin film at the edge than at the center (Fig. 4b). The coffee ring effect significantly influences the thin film morphology, homogeneity, and consequent device performance. Therefore, methods to suppress the coffee ring effect are highly important for inkjet-printed electronics.

Several approaches have been proven to be adequate in suppressing the coffee ring effect. Since the formation of the coffee ring mainly relies on solvent evaporation, increasing the solvent evaporation rate through decreasing environmental vapor pressure or increasing the drying temperature could effectively suppress the coffee ring effect.[31,32] Secondly, using mixed solvents with different boiling points and surface tensions could minimize the coffee ring effect.[33–36] When a mixed solvent was used, the low boiling pointing solvent would evaporate first, forming an outward flow in which the solvent would carry the solute towards the edge. In contrast, the use of a high boiling point solvent would form an inward flow to prevent the movement of the material circulation on the edge, which is known as the Marangoni flow. A balanced capillary flow and Marangoni flow will minimize the coffee ring effect. Sirringhaus et al.[37] proved the existence of an internal fluid flow in the ternary solvent through dynamic surface tension results (Fig. 4c), which might be indirect evidence of increasing the Marangoni fluid. Besides, the Marangoni flow effect could en-

hance molecular crystallization and regulate the film morphology.[38] Fig. 4(d) shows the two-dimensional grazing-incidence X-ray diffraction (2D-GIXD) images of the film prepared with pure solvent and composite solvents. Unlike the films from pure solvent, the film prepared with the addition of high-boiling point additive dodecane showed a stronger molecular orientation, which is conducive to charge extraction and transmission.

2.5 Film Formation

During inkjet printing, the droplets coalesce and form lines and films. Drop spacing (DS) influences the coalescence process significantly. Fig. 5 shows the droplet arrays with different drop spacings. Printing with large DS cannot form continuous lines and films while using small DS would create an overlap of droplets and consequently increase film thickness. Therefore, a proper DS is required to ensure appropriate droplet coalescence.
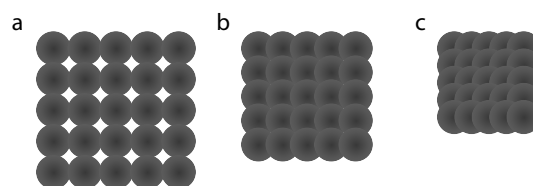
Fig. 5　Schematic representing different drop spacing: (a) large drop spacing cannot form continuous lines and films, (b) proper drop spacing, (c) small drop spacing forms thick films.

3 DEVELOPMENT OF INKJET-PRINTED ORGANIC SOLAR CELLS

In the last several years, inkjet-printed organic solar cells have developed tremendously. As shown in the summary of the recent development of inkjet-printed OSCs (Fig. 6), the efficiency of the inkjet-printed OSCs has improved quickly since 2019, mainly benefiting from the development of non-fullerene
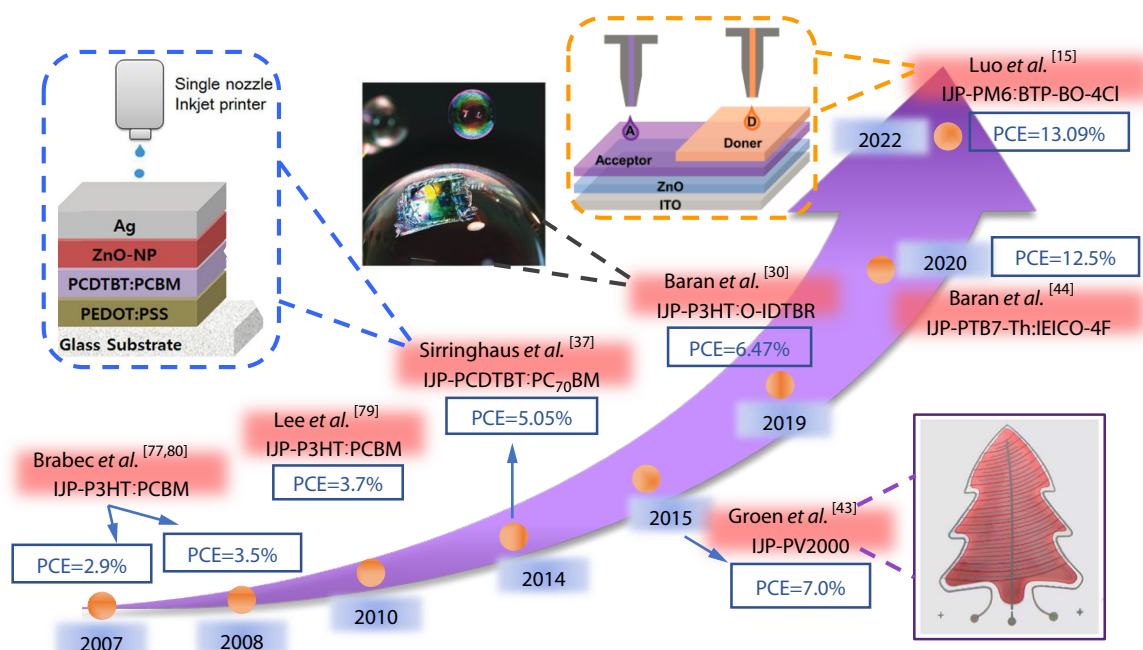
Fig. 6 Efficiency development of the organic solar cells with inkjet-printed photoactive layers.

acceptors. In 2005, Schubert et al.[41] successfully deposited organic photoactive layer by inkjet printing. Uniform and compact active layer films were obtained by using RuPMMA/$PC_{61}BM$ and RuPMMA/C7-V blends as the active layer. The UV-Vis absorption and photoluminescence spectra showed that inkjet-printed films have good optical properties. Although they did not fabricate devices with the printed organic thin films, this was the first attempt to prepare organic thin films by inkjet printing. Later in 2007, Brabec et al.[42] reported the inkjet-printed P3HT:$PC_{61}BM$ OSCs and achieved PCEs of 2.9% using a mixed solvent of ortho-dichlorobenzene (oDCB) and 1,3,5-trimethylbenzene (mesitylene). Following these pioneering works, several research groups devoted themselves to inkjet-printed OSCs. Although most of the printed OSCs are based on P3HT:$PC_{61}BM$ blend, the inkjet-printed cells showed a comparable photovoltaic performance to that of spin-coated cells, demonstrating the great application potential of inkjet printing in OSCs. In addition to the small-area devices with inkjet-printed photoactive layer, mini modules and fully inkjet-printed OSCs were also reported. For instance, fully-printed OSCs gave an efficiency of 4.1% for the PV2000 devices.[43] In 2014, Jung et al.[37] printed PCDTBT:$PC_{71}BM$ OSCs with a conventional structure of ITO/PEDOT:PSS/active layer/ZnO/ layer. They found that all the functional inks, including PEDOT:PSS, PCDTBT:$PC_{71}BM$, and ZnO, have suitable rheological properties. With a printed active layer, the device showed a performance of 5.05%, with an open-circuit voltage (V_{OC}) of 0.8 V, a short-circuit current density (J_{SC}) of 9.95 mA/cm^2 and a fill factor (FF) of 56.8%. In 2019, the first inkjet-printed non-fullerene OSCs with P3HT as the donor and rhodanine-benzothiadiazole-coupled indacenodithiophene (IDTBR) as acceptor were reported, which showed a record efficiency of 6.47%.[30] They regulated the printability and rheological properties by using oDCB and hydrocarbon-based inks and optimized the printing parameters and deposition temperature. Later on, the performance of IJP OSCs was further improved to

12.4% with poly[4,8-bis(5-(2-ethylhexyl)thiophen-2-yl)benzo [1,2-b;4,5-b′]dithiophene-2,6-diyl-alt-(4-(2-ethylhexyl)-3-fluo-rothieno[3,4-b]thiophene-)-2-carboxylate-2-6-diyl)] (PTB7-Th) and the low band gap 2,2′-[[4,4,9,9-tetrakis(4-hexylphenyl)-4,9-dihydro-s-indaceno[1,2-b:5,6-b′]dithiophene-2,7-diyl]bis[[4-[(2-ethylhexyl)oxy]-5,2-thiophenediyl]methylidyne(5,6-difluoro-3-oxo-1H-indene-2,1(3H)-diylidene)]]bis[propanedinitrile] (IEICO-4F) (PTB7-Th:IEICO-4F) active layer.[44] In addition, the device with a printed photoactive layer from xyl:Tel solvent also gave an efficiency of 9.8%. Recently, we demonstrated the layer-by-layer inkjet printing at high temperature could make a balance of vertical phase separation and molecular agglomeration, leading to high performance of non-fullerene PM6:BTP-BO-4Cl OSCs with efficiency of 13.09%.[15]

Most organic solar cells have a typical sandwich structure, where the photoactive layer is sandwiched between the an-ode and cathode. To smooth the charge injection and collec-tion at the electrode, charge transporting layers, including the electron transporting layer (ETL) and hole transporting layer (HTL) are usually used. Till now, all these functional lay-ers can be prepared by inkjet printing. This section will intro-duce the development of the inkjet-printed bottom elec-trode, ETL, the photoactive layer, HTL, and the top electrode. The materials involved in the inkjet-printed films are shown in Fig. 7. In summary, the Ag grid and AgNWs top electrode, the ITO/IZTO, CuNPs-PEDOT:PSS composite bottom electrode, the ZnO, AZO, PEDOT:PSS, and NiO charge transporting layer, as well as the organic photoactive layers were successfully prepared by inkjet printing.

3.1 Bottom Electrode

The commonly used bottom electrodes in OSCs include indium tin oxide (ITO),[45] indium zinc tin oxide (IZTO),[46] conductive polymers,[47] metal mesh,[48] metal nanowire mesh,[49] etc. ITO is the most widely used conductive electrode due to its advantages of high transmittance and low sheet resistance. ITO
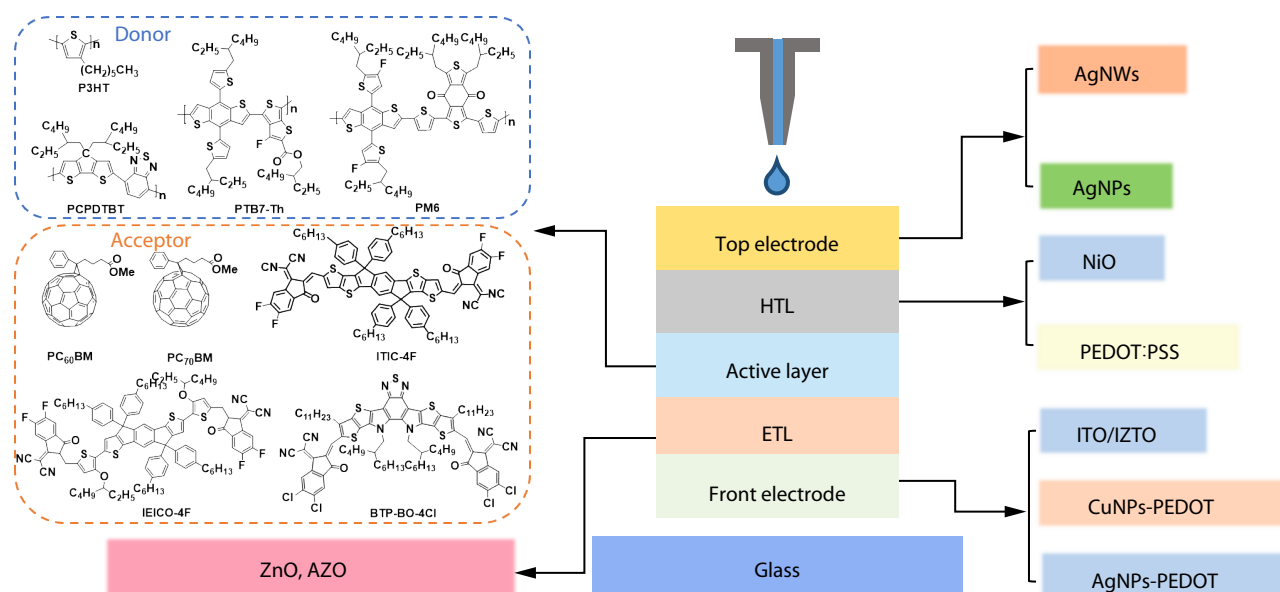
Fig. 7　Materials of functional layers are prepared by inkjet printing in organic solar cells.

electrodes are mainly prepared by magnetron sputtering. However, inkjet-printed ITO electrode was also reported. Kim *et al.*[45] inkjet-printed transparent ITO electrode from ethanol-dispersed ITO nanoparticles with a size of 25−30 nm. The printed ITO electrode showed a sheet resistance of 202.7 $\Omega/\square$ and a transmittance of 84.14%. Solar cells with a structure of glass/IJP-ITO/PEDOT:PSS/P3HT:PC$_{61}$BM/Ca/Al were fabricated and showed a PCE of 2.13%, which is lower when compared to the device using sputtered ITO electrode (3.78%). The lower device performance for the IJP-ITO-based cells can be attributed to the higher sheet resistance of the inkjet-printed ITO electrode. Despite this, this work proved the feasibility of preparing ITO electrodes by inkjet printing. Kim *et al.*[50] also prepared IZTO electrodes by inkjet printing. They optimized the drop spacing and found the film thickness increased with decreasing drop spacing since decreasing the drop spacing will increase the amount of inks. A film thickness of 1.5 μm was obtained at a drop spacing of 50 μm, which showed a sheet resistance of 21.6 $\Omega/\square$ and an optical transmittance of 81.29%. The IJP-IZTO/PEDOT:PSS/P3HT:PC$_{61}$BM/Ca/Al OSCs showed an efficiency of 0.81%.

Although ITO films based on rigid glass substrates showed excellent conductivity and transparency, flexible ITO films showed much higher sheet resistance of over 60 $\Omega/\square$, and they are not ideal for making large-area flexible solar cells. It is therefore essential to find alternative transparent electrodes to ITO films.[21,22,51] Conductive polymer composite, poly(3,4-ethylene dioxythiophene):polystyrenesulfonate (PEDOT:PSS) has the advantages of high optical transmittance and easy preparation. However, the sheet resistance of PEDOT:PSS is relatively high (100−200 $\Omega/\square$), which makes it unusable as a standalone electrode. Therefore, secondary dopants strategy is developed to improve the conductivity of PEDOT:PSS such as introducing organic solvents,[52,53] poly(alcohols),[54,55] or adding surfactants[56,57] and treating with acids.[58,59] Although the conductivity of PEDOT:PSS has been improved after the modification treatment, the devices yielded a poor PCE when using PEDOT:PSS as the bottom or the top electrodes in the organic solar cells.[60,61]

Composite electrode containing the metal-grids and PEDOT:PSS was then developed to address this problem.[47] Metal grids can be fabricated through thermal evaporation, screen printing, inkjet printing, and imprinting. Among these methods, inkjet printing has the advantages of high accuracy and low cost, thereby has been widely utilized in ITO-free organic solar cells. In this composite electrode, the conduction and light transmittance are mainly affected by the grid spacing. Galagan *et al.*[62] investigated the effect of metal grid line density on the performance of the device, and the sheet resistance of the composite electrode decreased from 20 $\Omega/\square$ to 1 $\Omega/\square$ as the grid space decreased from 20 mm to 1 mm. However, the increase in shadowing areas leads to an increase in shadowing loss. As an optimization, when the grid spacing was 2.5 mm, the composite electrodes achieved the best performance of 1.46% for the device with structure of IJP-Ag-grids/PEDOT:PSS/P3HT:PC$_{61}$BM/ LiF/Al with an area of 2 cm × 2 cm. Fig. 8(a) shows the calculated electrical potential and photographs of the current collection grids in the case of different grid spaces. It was apparent that the increase of grid number and decrease of grid spacing significantly improved the conduction. Using the metal grid electrode as the transparent conduction electrode, they found homogenous current distribution over the entire active area and apparent shadowing loss (Fig. 8b).

Moreover, the thickness of PEDOT:PSS layer would also influence the conductivity and light transparency of the electrode.[51] Therefore, the thickness of the PEDOT:PSS interface layer should be regulated correspondingly according to the thickness of the metal grid to lower interface charge recombination and improve FF. It was found that the inkjet-printed grid height increased from 400 nm to 600 nm when the drop spacing decreased from 30 μm to 15 μm. Consequently, the thickness of the PEDOT:PSS layer should be increased from 100 nm to 200 nm to better cover the Ag grids surface.
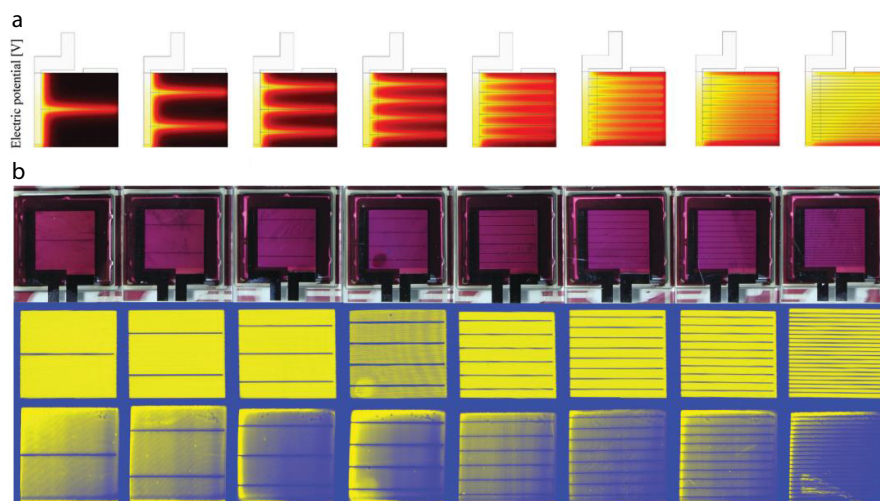
Fig. 8   (a) The calculated electric potential field for current collecting grids with different spacing at the working voltage of 0.4 V. (b) Photographic images of devices with lithographic current collection grids and light beam induced current images of the devices before and after the degradation. (Reproduced with permission from Ref. [62]; Copyright (2012) Wiley).

However, as the thickness increases, the transmittance of the bottom electrodes significantly decreases, leading to lower J_{SC}. As an optimized structure, the inkjet-printed Ag grid with a thickness of 400 nm was obtained with a drop spacing of 30 μm. Such a composite electrode showed a sheet resistance of 5–12 Ω/□, and the efficiency of 4 cm^2 OSCs reached 1.54% with a structure of IJP-Ag-grids/PEDOT:PSS/P3HT:PC$_{61}$BM/LiF/Al.[51] A big issue of the inkjet-printed electrode is the formation of the coffee ring structure. Choulis et al.[63] reduced the coffee ring effect by regulating the ink drop spacing (DS) and deposition temperature, and obtained Ag grids without apparent defects. Using high conductive PEDOT:PSS modification layer further realized comparable conduction with fewer grid numbers, thus ensuring higher transmission. Such an electrode was used in the glass/IJP-Ag-grids/PEDOT:PSS/P3HT/PC$_{61}$BM/Al device, giving an efficiency of 1.96%. In addition, Choulis et al.[64] used Ag nanoparticle inks that dispersed in the mixed solvents of ethanol and ethylene glycol for the IJP Ag electrode. The use of the mixed solvent, the coffee ring effect in the inkjet-printed Ag grid electrode was suppressed due to the Marangoni flow effect. The uniform Ag-girds were obtained by inkjet printing with a drop spacing of 35 μm and a substrate temperature of 35 °C. Thus, an efficiency of 4.9% is realized with the structure of Ag-grids/PEDOT:PSS/Si-PCPDTBT:PC$_{71}$BM/Al.

Owing to high conductivity and transparency, PEDOT:PSS has been widely used in small-area OSCs and obtained high efficiency as the replacement of ITO. However, when PEDOT:PSS was used in large-area devices, the PCEs were still limited due to the high sheet resistance. Although the conductivity of PEDOT:PSS was improved by various modifications,[65] it is still under-investigated to overcome the limitation of PCE caused by the large-area OPVs. Huang et al.[66] controlled the inkjet-printed Ag grids with a width of 200 μm and then increased the thickness of Ag grids by increasing printing cycles from 1 cycle to 3 cycles. The sheet resistance decreased from 5.8 Ω/□ to 2.7 Ω/□, as the printing cycles increased from 1 cycle to 3 cycles. Based on the optimized

inkjet-printed Ag girds, the high PCEs of 2.86%, 2.49% and 2.34% of ITO-free devices were achieved at the area of 0.3, 4 and 8 cm^2, respectively.

Though inkjet-printed grid electrodes have been widely used in OSCs, rare studies reported IJP transparent electrodes on flexible substrates. In 2012, Na et al.[48] successfully deposited Ag metal mesh on PET substrate by inkjet printing and prepared composite electrodes with PEDOT:PSS. The flexible composite electrode has a sheet resistance of 15.8 Ω/□ and transmittance at 550 nm of 82.51%. OSCs with the structure of PET/Ag-grids/PEDOT: PSS/P3HT:PCBM/Al:Ca showed a V_{OC} of 0.562 V, a J_{SC} of 6.30 mA/cm^2, an FF of 64.72%, and a PCE of 2.29%. Zhang et al. reported an Ag-grids/AgNWs/PEDOT three-layer composite electrode fabricated through inkjet printing with a sheet resistance of 16.5 Ω/□ and a transmittance of 87.5%. Such an electrode enabled a PCE of 3.26% when applied in the flexible organic solar cells.[67]

In addition to silver nanoparticles, Cu nanoparticles were used to prepare metal grid electrodes. For example, Georgiou et al.[68] reported a transparent Cu metal grid and PEDOT:PSS composite electrode prepared by inkjet printing (Fig. 9). Copper nanoparticles with a size of approximately 100 nm were used to prepare the ink, which has a viscosity of 12 cP and surface tension of 29–30 mN/m, showing excellent printability and stability. A drawback of copper nanoparticles was the undesired oxidation of copper in ambient conditions, particularly during thermal sintering, yielding increased resistance. To solve this problem, several approaches, including laser sintering and flash sintering were utilized as substitutes for thermal sintering. The printed grid was annealed through laser sintering. Through a systematical investigation of the relation between the conductivity of the copper film and laser sintering conditions, the optimized Cu grid electrode was achieved with a conductivity of 36000 S·cm^{-1} (sheet resistance of 500 mΩ/□) and a thickness of 450 nm when inkjet printed at a drop spacing of 25 μm.[68] Similar to the Ag grid, a thin PEDOT:PSS modification layer was needed to cover the Cu grid electrode to reduce short circuits and leakage. With
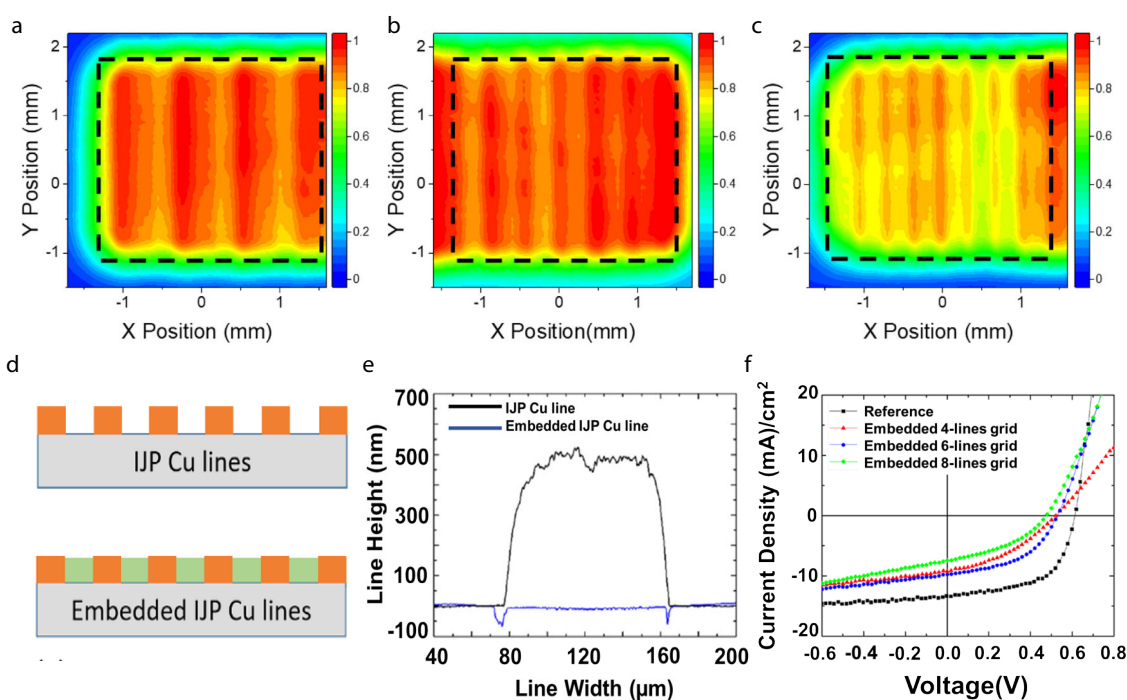
Fig. 9　Normalized photocurrent mapping images of OPVs with IJP Cu grid lines (a) 4 lines, (b) 6 lines and (c) 8 lines. Schematic view of Cu lines (d) before embedding (the first row) and after embedding (the second row). (e) Profilometry of IJP Cu lines before (black line) and after embedding (blue line). (f) Illuminated *J-V* characteristics of OPVs with different bottom contact. Reproduced with permission. (Reproduced with permission from Ref. [68]; Copyright (2018) Wiley).

Table 1　Electrode parameters of the cathode and anode prepared by inkjet printing and photoelectric properties of organic solar cells in literature.

Material	Device structure	Width/pitch size (µm/ mm)	Height (nm)	Sheet resistance (Ω/□)	Transmittance (%)	PCE (%)	Machine
ITO	Glass/ITO/PEDOT:PSS/P3HT:PC$_{61}$BM/Ca/Al	–	750	202.7	84.14	2.13	–[45]
IZTO	Glass/IZTO/PEDOT:PSS/P3HT:PC$_{61}$BM/Ca/Al	–	–	20.6	81.29	0.81	Unijet[50]
AgNPs	Glass/Ag-grids/PEDOT:PSS/P3HT:PC$_{61}$BM/ lif/Al	325/2.5	500	2.46	–	1.46	DMP2831[62]
AgNPs	Glass/Ag-grids/PEDOT:PSS/P3HT:PC$_{61}$BM/lif/Al	290/–	450	4.83	–	1.54	DMP2800[51]
AgNPs	Glass/Ag-grids/PEDOT:PSS/P3HT:PC$_{61}$BM/Al	46/0.7	200	–	92	1.96	DMP2832[63]
AgNPs	Glass/Ag-grids/PEDOT:PSS/Si-PCPDTBT:PC$_{71}$BM/Al	47/–	200	8.5	–	4.9	DMP2800[64]
AgNPs	Glass/Ag-grids/PEDOT:PSS/P3HT:PC$_{61}$BM /Al	47/–	200	8.5	–	2.8	DMP2800[64]
AgNPs	Glass/Ag-grids/PEDOT:PSS/P3HT:PC$_{61}$BM/Ca/Al	200/2	250	5.8	–	2.86	DMP2800[66]
AgNPs	PET/Ag-grids /PEDOT:PSS/P3HT: PC$_{61}$BM/Ca/Al	155/–	145	15.8	82.51	2.29	Omnijet 100[48]
AgNPs	PET/Ag-grids/agnws/PEDOT:PSS/P3HT:PC$_{61}$BM/BCP/Al	5–6/0.08	300	16.5	87.5	3.26	DMP2831[67]
CuNPs	Glass/Cu-grids/PEDOT:PSS/Si-PCPDTBT:PC$_{71}$BM/Ca/Al	80/0.43	450	0.5	–	3.35	DMP2800[68]

an optimized structure of Cu grid with grid width and grid space of 80–85 µm and 430 µm, togethering with a PEDOT:PSS cover layer, the Si-PCPDTBT:PC$_{70}$BM cell based on Cu grid/PEDOT:PSS composite electrode showed a PCE of 3.35%, with V_{OC}, J_{SC} and FF of 0.58 V, 11.39 mA/cm^2 and 50.72%, respectively. Similar to the silver grid electrode, uniform covering of IJP Cu grid by the active layer is a big challenge. To solve this problem, Georgiou *et al.* fabricated an embedded grid electrode through laser sintering, because the excessive heat from the laser would lead to the shrinkage of PET substrate and the formation of the embedded grid. An efficiency of 2.56% was obtained by optimizing the number of embedded IJP Cu lines (Figs. 9d–9f).[68]

Table 1 summarizes the research progress of inkjet-printed

bottom electrode and their application in organic solar cells. In summary, the inkjet-printed silver/copper metal grid electrodes showed comparable conductivity and light transparency to the ITO electrode, and OSCs with metal grid electrodes showed similar performance to the ITO devices. This result showed the great potential of the IJP bottom electrodes for application in OSCs, both in rigid and flexible devices.

3.2 Electron and Hole Transporting Layers

The commonly used electron transporting layer (ETL) materials in OSCs include polymers, metal oxides, and composite materials. ZnO is the most widely used ETL due to its high light transmittance and excellent electron conductivity. ZnO films are mainly prepared by spin-coating from a sol-gel precursor

solution[69] or a ZnO nanoparticle dispersion.[70] However, inkjet printing of ZnO films was also prepared. Garg *et al.*[71] systematically regulated the concentration and viscosity of the ZnO sol-gel solution and optimized the drop spacing and substrate temperature while printing ZnO inks. A high-quality 45 nm-thick ZnO film with a light transmittance of >85% was successfully achieved. In this case, the ZnO sol-gel solution comprised zinc acetate, 2-methoxyethanol, and mono ethanolamine as the stabilizing agent. The viscosity of ZnO sol-gel solution was increased from 2.07 cp to 4.70 cp by increasing the concentration from 0.25 mol/L to 0.70 mol/L, and the *Z* value was decreased from 14.02 to 5.62, making it more suitable for inkjet printing. They demonstrated that spherical droplets without tails were obtained only with a *Z* value of 5.62, corresponding to a precursor concentration of 0.7 mol/L. Sacramento *et al.*[72] used inkjet-printed ZnO in OSCs and achieved a higher efficiency of 5.64%. The ZnO inks were crystalline ZnO nanoparticles with a size of 12±4 nm that dispersed at 2.5 wt% in isopropanol and propylene glycol composite solvent with a viscosity of 11±3 mPa·s. The device showed better stability than the conventional poly[(9,9-bis(3'-(*N*,*N*-dimethylamino)propyl)-2,7-fluorene)-*alt*-(2,7)9,9-dioctyl-fluorene] (PFN) ETL-based devices, demonstrating the feasibility of a large-area printing ZnO electron transporting layer.

Commonly used hole transporting layer (HTL) in OSCs include PEDOT:PSS, PEDOT-F[75] and metal oxides, like MoO$_3$

and NiO. Particularly, PEDOT-F has excellent film formation quality on the top of the active layer, showing great potential for fully-printed OSCs. Inkjet-printed PEDOT:PSS HTL has been extensively studied and applied in OLED devices. However, it is challenging to print PEDOT:PSS HTL on the top of the photon active organic layer due to the mismatch of surface energy. As shown in Fig. 10, the PEDOT:PSS films did not cover the active layer. Therefore, a formulation of aqueous PEDOT:PSS with the addition of various surfactants was reported for inkjet printing.[73] The contact angle of the modified PEDOT:PSS on the P3HT:PCBM layer showed the addition of surfactants decreased the surface energy and promoted the film quality of PEDOTS:PSS HTL through inkjet printing.

Owing to the hydroscopic nature of PEDOT:PSS, the cells based on PEDOT:PSS usually showed low-performance stability. In contrast, metal oxide HTL will ensure better stability of the cell. So, several works reported the inkjet printing of metal oxide HTL for OSCs. For instance, Singh *et al.*[74] inkjet-printed NiO from a precursor ink with controlled thickness and morphology by systematically optimizing the printing DS, substrate temperature, and annealing temperature. As shown in Fig. 11, the surface of the films with the drop spacing of 30, 40 and 60 µm was not uniform, while the film printed at 50 µm was much smooth. Meanwhile, the increasing of substrate temperature from 25 °C to 55 °C led to a rough film as
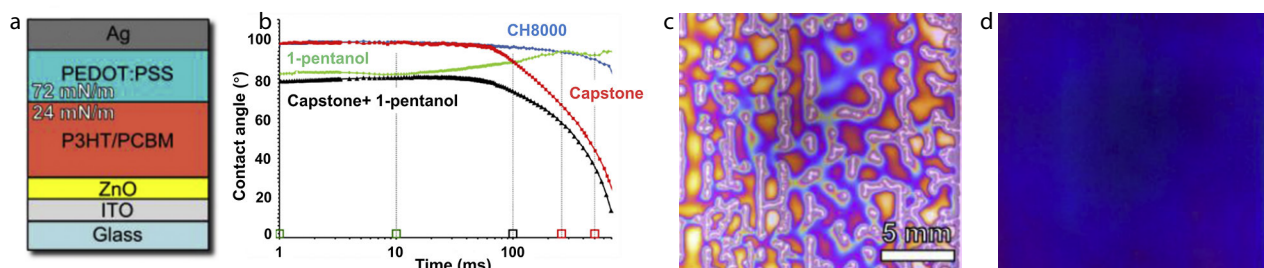
Fig. 10 (a) The structure of the inverted OSCs. (b) Dynamic contact angles of the PEDOT:PSS with different formulations. The photographs of the inkjet-printed PEDOT:PSS layers on the top of P3HT/PCBM without (c) and with (d) surfactants. (Reproduced with permission from Ref. [73]; Copyright (2018) Elsevier).
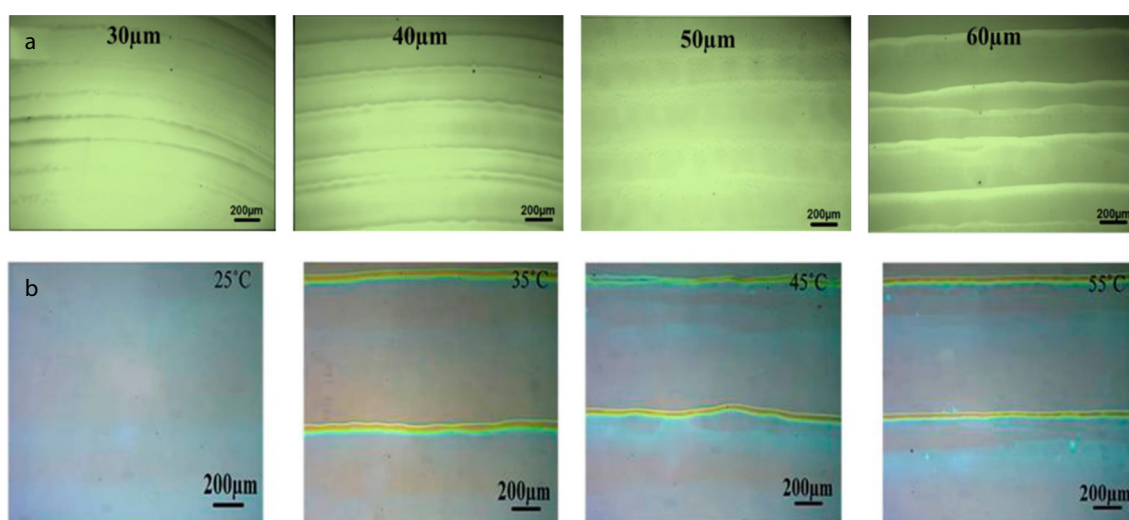
Fig. 11 The optical images of inkjet-printed films processed by different drop spacing (a) and (b) substrate temperatures. (Reproduced with permission from Ref. [74]; Copyright (2017) Science Reports).

Table 2 Ink formulation of the electron and hole transport layer and printing parameters in literature.

Materials	Solvent	DS (μm)	Thickness (nm)	Temperature (°C)	Machine
ETL-ZnO	2-Methoxyethanol	45	25	25	DMP2831 [71]
ETL-ZnO	Isopropanol, propylene glycol	15	100	30	DMP2800 [72]
HTL-PEDOT:PSS	Water	20	200		KM512LN [73]
HTL-NiO	2-Methoxyethanol	50	18	25	DMP2831 [74]

well. The printed NiO films have a transmittance of 89% with a uniform structure and morphology. The NiO precursor inks used for IJP have a surface tension of 36.9 mN/m and a viscosity of 2.6 cP. The corresponding Z number was 11.4. The OSCs with printed NiO HTL exhibited a high power conversion efficiency compared to devices with spin-coated NiO films and significantly enhanced performance and stability compared with the PEDOT:PSS HTL device. We also summary the ink formation and printing process in Table 2.

3.3 Organic Photoactive Layer

Nowadays, the record efficiency of single-junction OSCs has exceeded 19%, with a small area of <0.1 cm² prepared by spin-coating. Transferring the state-to-art process to large-area roll-to-roll printing is critical for commercializing OSCs. In recent years, the development of inkjet-printed OSCs shows great application potential in the fabrication of active layers through IJP. Fig. 12 summarizes the molecular structures of the organic donors and acceptors those have been successfully fabricated

through inkjet-printing, including P3HT, PCPDTBT, PTB7-Th, PBDB-T, PM6, PC$_{61}$BM, PC$_{71}$BM, IEICO-4F, ITIC, ITIC-4F and BTP-BO-4Cl. Totally speaking, the difficulties in inkjet printing the photoactive layer include inhibiting coffee rings and controlling nanophase separation morphology. Inkjet printing requires stable ink, thereby solvents with high boiling points are usually used. However, most of the non-fullerene acceptors exhibited excessed aggregation in high boiling point solvent, which limited the performance of the devices. In this section, the development of inkjet printing of active layer, the influence of ink physical properties and printing parameters on the micromorphology of thin-film, and device performance will be summarized in detail.

Like most of the various printing processes, inks, substrate and technology are the three printing factors for the inkjet-printing. The detailed relationship among inks, substrates, and printing technologies is shown in Fig. 13. Specifically, the ink rheology property is a basic that decides the droplet ejec-
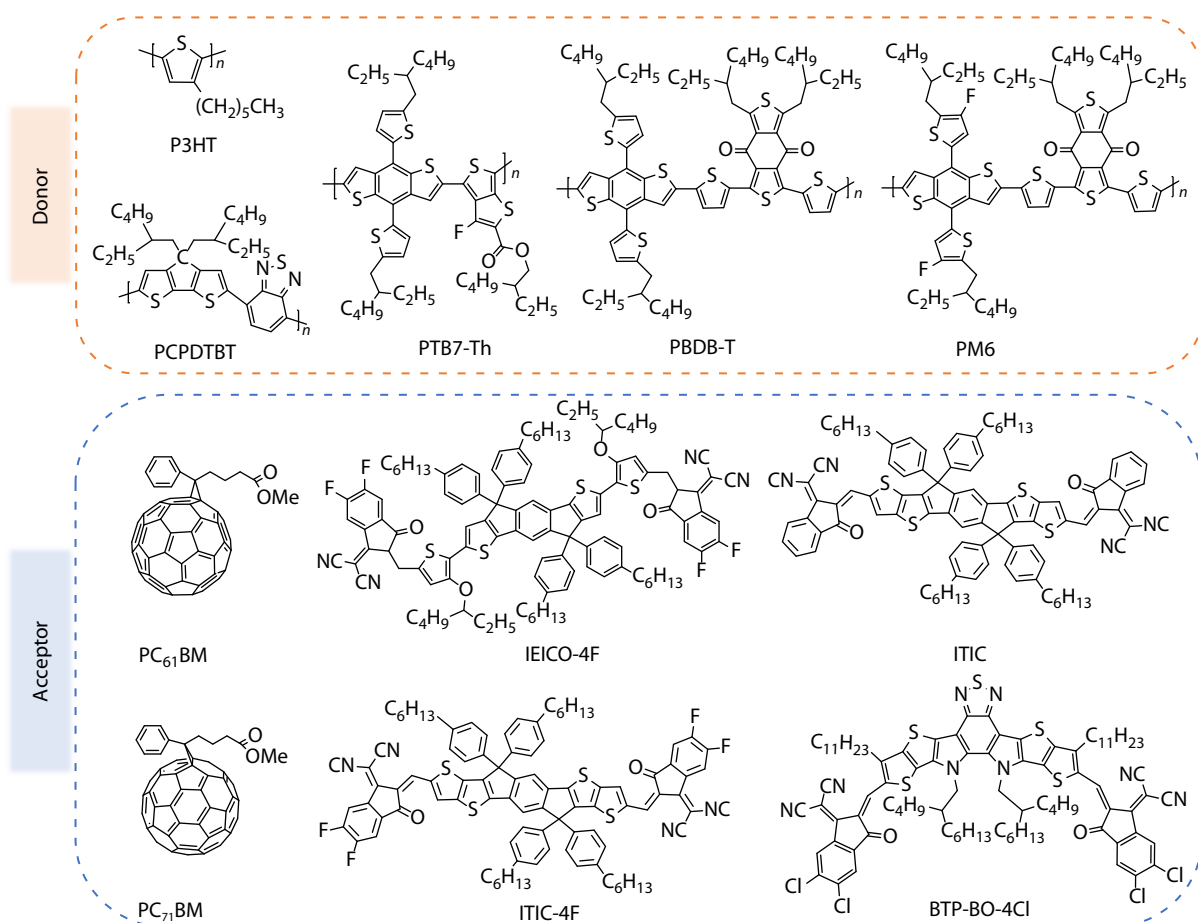
Fig. 12 Molecular structures of the organic donors and acceptors utilized in inkjet-printed OSCs.
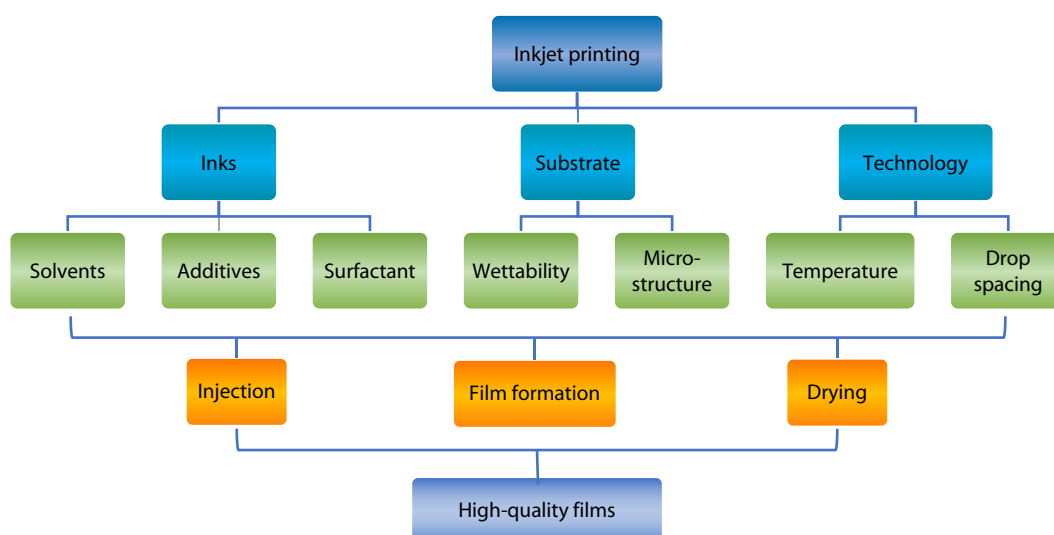
Fig. 13   The main aspects that impact the film quality from inkjet-printing and the correlation.

tion, ink leveling and drying. The substrates highly influence the inks leveling, and subsequently the film morphology. Therefore, the ink rheology property, substrate surface energy and printing technology are always systematically regulated during inkjet-printing.

3.3.1 Ink formulation

The rheological properties of inks were mainly regulated by solvent, concentration, and additive. Although most high-performance organic solar cells were fabricated by spin-coating using low boiling point solvents, the low boiling point solvents are not suitable for inkjet printing. Thus, the first issue is the solvents used in spin-coating cannot be directly transferred to the inkjet printing route. To ensure stable droplet ejection without nozzle blocking, the main solvents for inkjet printing should have relatively high boiling points. Till now, chlorobenzene (CB), *ortho*-dichlorobenzene (*o*DCB), trimethyl benzene (TMB), and indan are the most frequently used solvents for the preparation of photoactive ink for inkjet printing.[42,44,76]

The ink droplets should have appropriate fluidity and good wettability with the substrate to ensure good droplet coalescence, which is crucial for achieving a high-quality wet film. In the meanwhile, a balance of droplet drying and coalescence is key to determining film quality. Therefore, surface energy, viscosity and drying speed of the solvent are important for ink formulation for inkjet printing. Aernouts *et al.*[77] investigated the influence of the P3HT:PC$_{61}$BM concentration on the film morphology of the inkjet-printed thin film. They found that the adjacent lines were well fused and formed a smooth and continuous film using 1 wt% ink solution. This was due to the excellent wetting between the solution and the substrate. The 2 wt% ink solution has a high viscosity, yielding a poor ink droplet spreading and, thus, a rough surface. With 1 wt% P3HT:PC$_{61}$BM solution, ITO/PEDOT:PSS/P3HT/PC$_{61}$BM/Al devices gave an optimal device performance of 1.4%. Choulis *et al.*[42] investigated the influence of the mixed solvent of mesitylene and *o*DCB on the quality of the P3HT:PC$_{61}$BM thin film. The proportion of the two solvents remarkably influenced ink printability. With a concentration of mesitylene less than 32% in the mixture solvent, the inks have poor wetting

and spreading ability on the substrates. In contrast, a higher percentage of mesitylene resulted in lower solubility of materials and poor printing reliability.

Also, ink viscosity determines the formation of droplets and the drying process of the wet films. Mixing high-molecular-weight polymer within the ink is an effective method to regulate the viscosity of the ink. Eggenhuisen *et al.*[76] reported the use of polystyrene as an additive in P3HT/PC$_{61}$BM to improve the viscosity of the ink using 1,2,3,4-tetrahydronapthalene, indan and *o*-xylene mixture non-halogenated solvent. The influence of polystyrene (PS) molecular weight and blending concentration on the final device performance was investigated. By blending with 1 wt% of PS with low, middle, and high molecular weight, the viscosity of ink increased from 1.3 mPa·s to 1.6 mPa·s, 2.4 mPa·s and 2.9 mPa·s, respectively. However, the viscoelastic ink behavior occurred in such inks with high viscosity (2.9 mPa·s), which impacted the ink ejection. At the same time, the poor miscibility of PS and P3HT:PC$_{61}$BM led to a significant decrease in J_{SC}. Although mixing PS caused a reduction of efficiency, a simple method was provided to improve the processability of photoactive materials and non-halogenated solvents.

In addition to solvents, the structure of polymers also showed a significant influence on the final device performance. Brabec *et al.*[78] compared the influence of the regularity of the P3HT on the P3HT:PC$_{61}$BM cells performance prepared by spin-coating, doctor-blade coating, and inkjet printing. Results showed that, for the doctor-blade coated cells, the high molecular regularity of P3HT is favorable for higher device performance, which is similar to the spin-coated cells and was attributed to a better crystallization of P3HT within the blend. However, for inkjet-printed cells, the use of higher molecular regularity of P3HT (RR=98.5%) decreased the cells performance owing to more severe molecular aggregates of P3HT relative to the molecular with low regularity. The different impacts of molecular regularity on the device performance between spin/doctor-bladed and inkjet-printed films were attributed to the drying speed of different processes. The relatively slower dying speed of ink-jet printing en-

hanced molecular aggregates for P3HT with higher regularity. With the optimization of molecular regularity and solvent mixture, a high-performance (with a PCE of 3.5%) P3HT:PC$_{61}$BM cells were prepared using P3HT (RR=96%) and a mixed solvent of *o*DCB/TMB (68:32, *V:V*), which was comparable to that of the spin-coated cells.

High-performance OSCs from spin-coating are generally processed with halogen solvents, which are toxic and hazardous. For future roll-to-roll mass production, halogen-free solvents are needed. As for the non-toxic solvents for OSC fabrication, the solubility of the active materials in these solvents and the viscosity of the final inks are the key factors affecting ink rheology. Most organic semiconductor materials have low solubility in non-halogen solvents, which generally leads to insufficient layer thickness. Mixed non-halogen solvents and halogenated solvents were used in inkjet printing. In 2020, Baran and Corzo *et al.*[44] prepared PTB7-Th:IE-ICO-4F devices through inkjet printing, and an efficiency of 12.44% and 9.88% was achieved for devices using CB:CN and *o*DCB solvent. With xylene and tetraline solvent, the device presented a performance of 9.8%. At the same time, they also prepared fully printed semitransparent organic solar cells with printed silver nanowire top electrodes, which showed average visible transmittance of 50.1% and a PCE of 9.5%. In all, the ink formulation, the printing parameters, and the device performance are listed in Table 3.

3.3.2 Interface wettability

Besides the ink formulation and printing processing, wettability between the ink droplets and substrates also directly impacts the film formation and influences the film quality and performance. During the fabrication process of OSCs, wettability issues existed between all the interfaces of different functional layers. Since physical treatment methods, such as UV-ozone, plasma and corona, can be applied directly to the electrode, the wettability between the ink and the electrode can be easily tuned. For instance, Garg *et al.*[71] found that surface treatment

of the ITO substrates through UVO for 15 min greatly improved the wettability of ZnO inks on the substrate and helped droplets spread, which consequently yielded a uniform film. Fig. 14 shows the optical micrographs of the printed ZnO films on the pristine and UVO-treated substrates. The reduction of contact angle indicated the practical impact of UVO treatment to improve surface wettability, leading to homogenous films.

However, the wettability between different functional layers could be more problematic since the regular physical surface treatments directly onto the functional layer would cause damage to the functional layer. Instead, the wettability issues between the functional layers are usually solved through ink engineering, materials engineering, and chemical surface treating routes. The inkjet inks generally should have proper surface tension around 30–50 mN/m. More importantly, the surface tension should be compatible with the substrate and the underneath layer. When printing the active layer on top of the PEDOT:PSS layer, Hoth *et al.*[42] found that due to the low surface energy of PEDOT:PSS, *o*DCB with high surface tension (37 mN/m) has poor interface contact with PEDOT:PSS, which was not beneficial to the film formation. Thus, they have reduced dehumidification behavior of the active layer on PE-DOT:PSS interface by using a low surface tension solvent trimethylbenzene (28.8 mN/m) as a substitute. However, when the proportion of trimethylbenzene was higher than 32% in the mixture solvent, the P3HT:PC$_{61}$BM showed poor solubility. Finally, the optimized device of ITO/PEDOT:PSS/P3HT: PC$_{61}$BM/Ca/Ag gave an efficiency of 2.9%. A severe wettability issue existed in the inverted OSCs, where hydrophilic PEDOT:PSS is deposited directly onto the hydrophilic polymer surface. Ma *et al.* found a composite hole transporting ink of PEDOT:PSS and MoO$_3$ nanoparticles could be easily deposited on the top organic layer without any specific physical treatment.[86,87] A similar route might also be workable during inkjet printing.

Table 3 Ink formulation of the active layer and performance of organic solar cells in literature.

| Active layer	Solvent	DS (µm)	Thickness (nm)	Temperature (°C)	PCE (%)	Machine
P3HT:PCBM	CB, tetraline	120	120		1.4	DMP2831 [77]
PCPDTBT:mono-PCBM	CB, *o*DCB		100		1.48	AD-K-501 [79]
P3HT:PCBM	CB, 1,8 octanedithiol		150	26	3.71	UJ2100 [80]
P3HT:PCBM	*o*-Xylene, indane, tetraline	30	200	80	1.75	PIXDRO LP50 [76]
P3HT:PCBM	*o*DCB, mesitylene		200	40	2.9	DMP 2831 [81]
P3HT:PCBM	*o*DCB, mesitylene		230	40	3.5	DMP 2831 [78]
P3HT:*o*-IDTBR	*o*DCB	10	260	60	6.47	DMP 2800 [30]
P3HT:ICBA	*o*DCB		170	30	4.7	– [82]
P3HT:PCBM	CB, tetraline		115		3.2	DMP 2831 [71]
P3HT:PCBM	*o*-Xylene, indane, tetraline		240		2.09	KM512L [83]
P3HT:PCBM	*o*-Xylene, indane, tetraline		240		0.95	KM512L [83]
PV 2000			260		7.0	DMP 2831 [43]
P3HT:PC$_{60}$BM	*o*-Xylene, indane, tetraline		240		2.2	DMP 2831 [43]
PTB7-Th:IEICO-4F	CB	30	100	20	9.65	DMP 2800 [44]
PTB7-Th:IEICO-4F	CB:CN	30	100	20	12.44	DMP 2800 [44]
PTB7-Th:IEICO-4F	*o*DCB	30	100	20	9.88	DMP 2800 [44]
PTB7-Th:IEICO-4F	*o*-Xylene, tetraline	30	100	20	9.80	DMP 2800 [44]
PM6:ITIC-4F	*o*-Xylene, tetraline	35	120		10.12	Ardeje Origind100 [84]
p-DTS(FBTTh$_2$)$_2$:PC$_{70}$BM	CB:DIO			50	7.3	MicroFab [85]
PBDB-T:ITIC	*o*DCB	40	140	50	6.43	DMP 2850 [15]
PM6:BTP-BO-4Cl	*o*DCB	40	130	50	13.09	DMP 2850 [15]
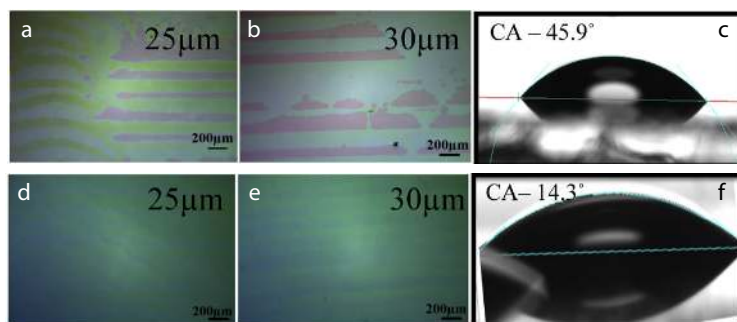
Fig. 14 Optical micrographs of printed films on the pristine (a, b) and the UVO (d, e) treated substrates and the contact angle of the inks on the top of the pristine (c) and UVO (f) treated films. (Reproduced with permission from Ref. [71]; Copyright (2018) Elsevier.)

3.3.3 Mesoscopic morphology and coffee ring control

The mesoscopic morphology of the blend films should be considered carefully when inkjet printing organic thin films. During inkjet printing, the mesoscopic morphology of the films was impacted by printing drop spacing, printing temperatures, and printing speed. Regarding this, selecting a proper solvent is essential. Figs. 15(a) and 15(b) show the PCDTBT:PC$_{71}$BM films inkjet-printed from the CB solvent, which is rough and not continuous. In contrast, a homogenous film was successfully achieved by replacing CB with a ternary solvent of mesitylene, chlorobenzene, and chloroform for ink formulation. Fig. 15(c) shows the *J-V* curves of the devices printed using different solvents. The devices using a ternary solvent of mesitylene, chlorobenzene, and chloroform exhibited the best performance. Corzo *et al.*[30] used P3HT:O-IDTBR as the active layer and optimized the micromorphology by regulating printing parameters, substrate temperature, and drop spacing. As shown in Fig. 15(d), the mesoscopic morphology of thin films was simultaneously influenced by substrate temperatures and drop spacing. Compact and continuous films were formed with substrate temperatures lower than 50 °C when the printing dot spacing is smaller than 10 μm. Particularly, when the temperature decreased to lower than 30 °C, the films were quite rough with root-mean-square around 16–20 nm. However, as increasing the temperature to 50 or 60 °C, some overlap lines were observed because the printed lines dried before connecting with the next line. Optimized DS of 10 μm and temperature of 40–50 °C were chosen to form uniform films. Finally, based on the optimized process, the device with an efficiency of 6.47% was successfully prepared. When the device area was enlarged to 2 cm^2, the efficiency was still kept at 6%. Such a small efficiency loss during upscaling from small to large-area devices proved the films prepared by inkjet printing have good uniformity. Figs. 15(e) and 15(f) present DS and temperature-dependent device performances. DS mainly influenced J_{SC} and FF, while substrate temperature mainly impacted FF. The influence of DS could be attributed to thickness difference, and the influence of substrate temperature was due to film temperature.

3.3.4 Nanophase separation morphology controlling

For the heterojunction organic solar cells, the device performance is highly impacted by the nano morphology of the films, which is usually adjusted by solvents and additives. Usually, the nano morphology was adjusted through solvents and additives engineering. Taking the P3HT:PC$_{61}$BM device as

an example, printing trials were observed using a single tetralin solvent and showed a rough film and strong phase separation of P3HT and PC$_{61}$BM. Using a mixed solvent of *ortho*-dichlorobenzene and mesitylene led to improved film quality due to reducing in dying time. Schubert *et al.*[79] dissolved several organic active layers, *i.e.*, PCPDTBT:bis-PC$_{61}$BM, PCPDTBT:mono-PC$_{61}$BM, PSBTBT:mono-PC$_{61}$BM in the mixed solvent of CB and *o*DCB, and found only with suitable CB/*o*DCB ratio (90:10), the films showed low roughness. Higher CB or *o*DCB content resulted in inhomogeneous films. Particularly, inks with a higher proportion of *o*DCB were more likely to form a coffee ring. In comparing the performance of PCPDTBT and PSBTBT donors-based devices, the PCPDTBT-based devices showed better performance than the PSBTBT device. This was mainly ascribed to the low solubility of PSBTBT in the solvent, which leads to large-scale aggregation during film drying. The device with the structure of ITO/PEDOT:PSS/PCPDTBT: mono-PC$_{61}$BM/LiF/Al showed a PCE of 1.48%. The high boiling point additive can enhance the Marangini fluid effect and promote molecular crystallization to form an optimized morphology. Lee *et al.*[80] printed P3HT:PC$_{61}$BM films with CB as the primary solvent and 5 vol% 1,8-octanedithiol (ODT), *o*DCB, and chloronalin (CN) as additives. The film surface roughness without additives was 60 nm, and the roughness of the film with additives was around 20 nm (Fig. 16). The reduce of film surface roughness was effective to improve the device performance. Thus, compared with the films without additives, doping of 1,8-octanedithiol in *o*DCB improved the lower short-circuit current and photoelectric conversion efficiency, consequently, the device efficiency improved from 1.97% to 3.71% through using the additives.

For the printed OSCs, regulating the film morphology is vital in engineering to improve the device performance and stability. Generally, a balance phase separation of donor and acceptor with proper phase separation size and purity is required. Several methods have been developed to manipulate the morphology, including solvent-additive engineering, annealing, as well as novel deposition strategies. For the inkjet-printed active layer, it is more complex and challenging to manipulate the nano morphology of the active layer. During inkjet printing, slower drying kinetics compared to spin-coating made the phase separation more significant. Different surface and bulk morphologies have been found in the inkjet-printed and spin-coated films. For instance, Ackermann *et al.* found that a PM6 capping layer was formed on the surface of
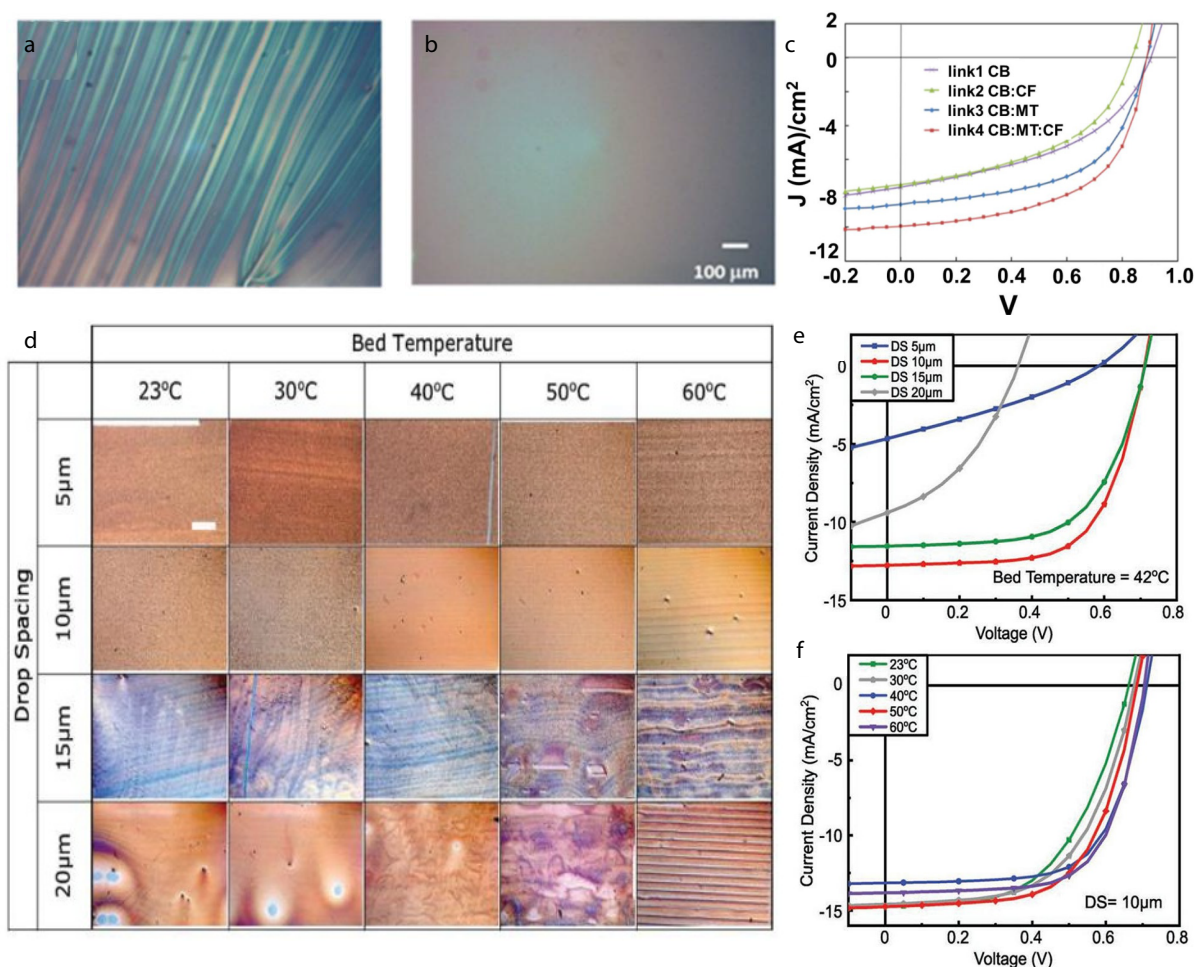
Fig. 15　(a, b) Microscopy images of inkjet-printed PCDTBT:PC$_{71}$BM blend layers formed solutions in chlorobenzene and ternary solvent, respectively. (c) *J-V* curves of cells printed with different solvents. (Reproduced with permission from Ref. [37]; Copyright (2014) Wiley). (d) Optical microscope images of films printed by inkjet printing with different substrate temperatures and drop spacing at 500 Magnification. Scale bar = 500 μm; (e) *J-V* curves of cells printed at different drop spacing at a constant substrate temperature of 42 °C; (f) *J-V* curves of cells printed with fixed drop spacing of 10 μm and varying substrate temperature. (Reproduced with permission from Ref. [30]; Copyright (2019) Wiley).

the photoactive film when inkjet printing PM6:ITIC-4F active layer (Figs. 17a and 17b), which was different from the spin-coated films (Figs. 17c and 17d). As shown in Figs. 17(c) and 17(d), the inkjet-printed films showed a higher roughness (1.7 nm) in comparison with spin-coated films (0.7 nm), while a fibril pattern was also observed. The ATEM results also verified the formation of PM6 capping layer on the surface of the printed films (Figs. 17b and 17d). Meanwhile, the water contact angle of spin-coated and inkjet-printed films was 92° and 100° (Figs. 17e and 17f), which indicated the fraction of PM6 on the surface of the spin-coated and inkjet-printed blend films is 33.42% and 77.98%, respectively.[84]

Meanwhile, substrate temperature and printing speed are other important factors that impact film morphology. Lan *et al.*[85] (Figs. 18a−18f) found that when the substrate temperature was lower than 50 °C, the crystal size was much larger than the crystal size of film printed at 80 °C due to slower drying speed during deposition. It was also found that the crystal size of the active layer decreased from 23.6 nm to 19.7 nm with increasing inkjet printing speed from 20 mm/s to 60

mm/s at the substrate temperature of 50 °C, which was due to the shorter drying time of the active layer with a faster inkjet printing speed. Similarly, the crystal size decreased from 19.7 nm to 18.8 nm as the inkjet printing speed increased at a substrate temperature of 80 °C. More importantly, the crystal size of the active layer processed at 80 °C significantly decreased compared to the sample processed from a substrate temperature of 50 °C with the same inkjet printing speed. When the substrate temperature was 50 °C, the device fabricated from low printing speed obtained a PCE of 4.3% with a V_{OC} of 0.81 V, a J_{SC} of 8.4 mA/cm^2, and an FF of 63.9%. The device from medium inkjet printing speed showed an improved performance of 7.3%. This work showed the significant effect of velocity and substrate temperature on the morphology of the active layer. The donor crystallization is significantly impacted by printing speed and substrate temperature. A possible mechanism was described in Figs. 18(g)−18(l).

Due to the difference in film formation and drying behavior between inkjet printing and spin-coating, the regulation of bulk heterojunction morphology becomes more complex and
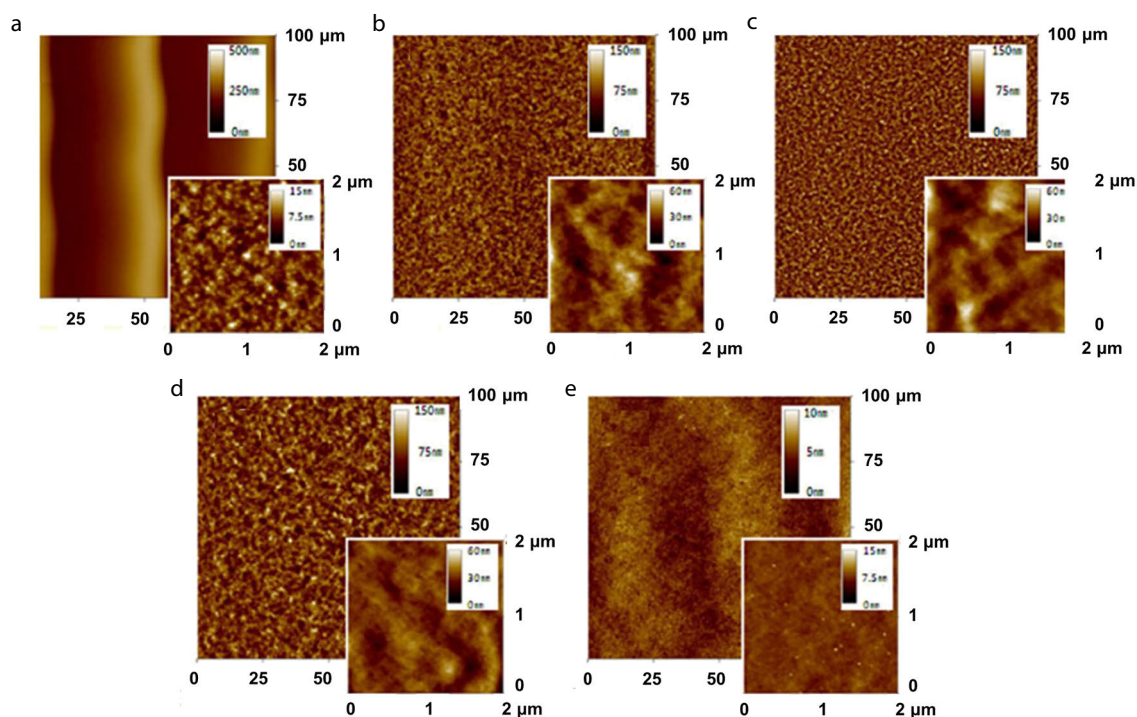
Fig. 16　AFM images of the P3HT:PC$_{61}$BM active layers fabricated from different high boiling point additives: inkjet-printed (a) CB (b) 5 vol% ODT (c) 5 vol% oDCB (d) 5 vol% CN and (e) spin-coated CB. (Reproduced with permission from Ref. [80]; Copyright (2010) Elsevier).
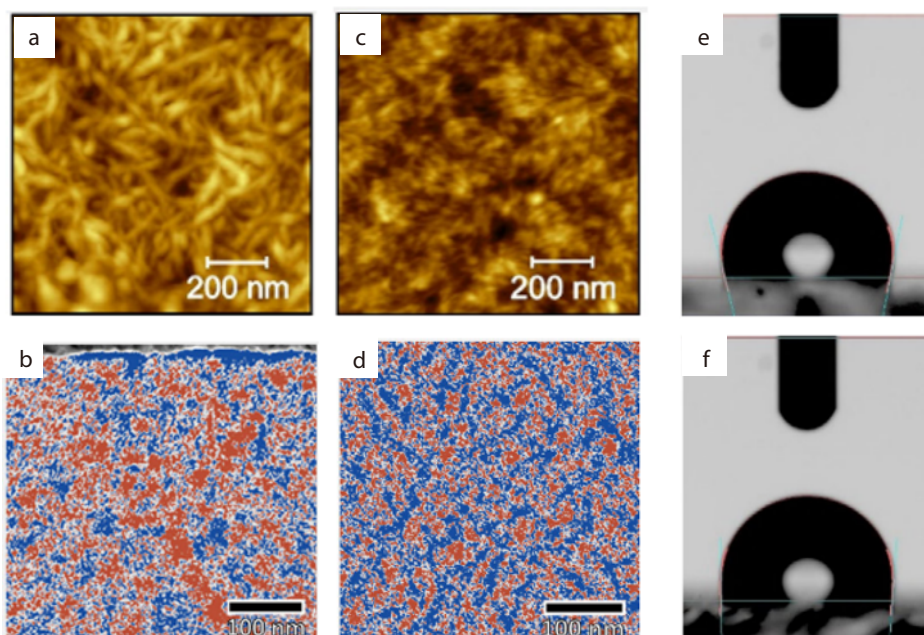

Fig. 17　AFM, ATEM and contact angle analysis of PM6:ITIC-4F (a, b, e) inkjet-printed and (c, d, f) spin-coated films. (Reproduced with permission from Ref. [84]; Copyright (2021) Wiley).

difficult when transferring spin-coating to printing. Luo *et al.*[15] demonstrated a layer-by-layer inkjet-printing (LbL-IJP) strategy (Fig. 19a) to balance vertical nanophase separation and molecular aggregation. When printing at low temperatures by one-step route, the films exhibited gradient vertical nanophase separation structure and larger molecular aggregates. However, when printing at high temperatures, the films exhibited a homogenous vertical nanophase separation structure and smaller surface roughness (Figs. 19b and 19c), which is unlike the spin-coated films with organic donor and acceptors formed local enrichment at anode and cathode interface (Figs. 19d–19g). Thus, they provided the LbL-IJP strategy to control the vertical and plane nanomorphology of the photoactive layer, which printing the acceptor and donor
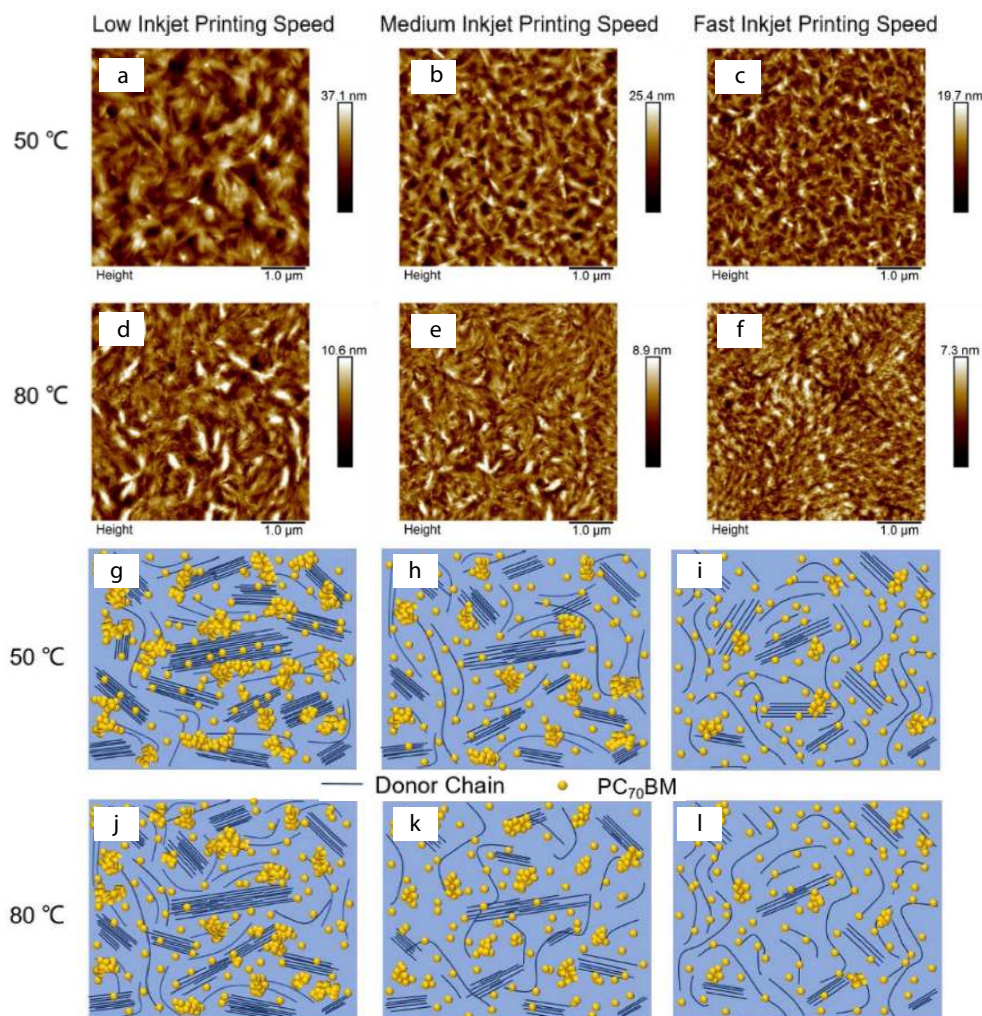
Fig. 18 (a–f) AFM surface morphology and (g–l) schematic of the nanomorphology of the active layer from different inkjet printing speeds and substrate temperatures. (Reproduced with permission from Ref. [85]; Copyright (2021) IOP).

sequentially. Using LbL-IJP film, they obtained a recorded efficiency of 13.09% for the OSCs with inkjet-printed PM6:BTP-BO-4Cl organic photoactive layer.

3.4 Top Electrode

The commonly used top electrodes for OSCs include Al, Ag, Au, metal nanowires (AgNWs), and conductive polymer PEDOT:PSS.[88,89] At present, Al/Ag are mainly deposited by vacuum thermal evaporation. In comparison with thermal evaporation, inkjet printing can significantly improve production efficiency and reduce manufacturing costs. However, only a few works were reported on inkjet-printed top electrodes. Galagan et al.[90] successfully deposited dense Ag and Ag grid transparent electrodes on the surface of PEDOT:PSS by inkjet printing AgNPs (average transmittance >80%). With optimization of thickness, opaque and semitransparent devices showed an efficiency of 2.8% and 2.7%. Choulis et al.[91] studied the influence of Ag nanoparticles diameter and solid content on device performance and found that using the mixture of 80% EMD5603 (Ag nanoparticle <150 nm size and 20% solids content dispersed in ethylene glycol) and 20% AgNP (<50 nm size and 30%–35% solids) could effectively improve the

electrode conductivity. Devices with an efficiency of 2.89% were obtained with such a printed electrode.

AgNWs have attracted much attention due to their high flexibility, conductivity, and transparency, as well as the advantages of simultaneous solution processing. There are several routes to prepare silver nanowire electrodes. Nevertheless, as the top electrode, non-contact printing would be more suitable because it will not affect the active layer. In 2015, Ma et al.[92] prepared transparent silver nanowires top electrode for OSC through inkjet printing. The electrode transmittance and conductivity highly impacted the performance of semitransparent electrodes. However, it is contradictory that increasing printing times is beneficial to improve the conductivity and will reduce the transmittance of the electrode, and vice versa. As shown in Fig. 20(a), the absorbance of solar cells increased with the increase of printing times, due to the decrease in transparency of Ag NW electrode. And the semi-transparent devices showed an average transparency of 57% over the entire visible wavelength (Fig. 20b). Finally, the optimized OSCs yielded an efficiency of 2.7% with inkjet-printed Ag NWs electrode (Fig. 20c). During the print-
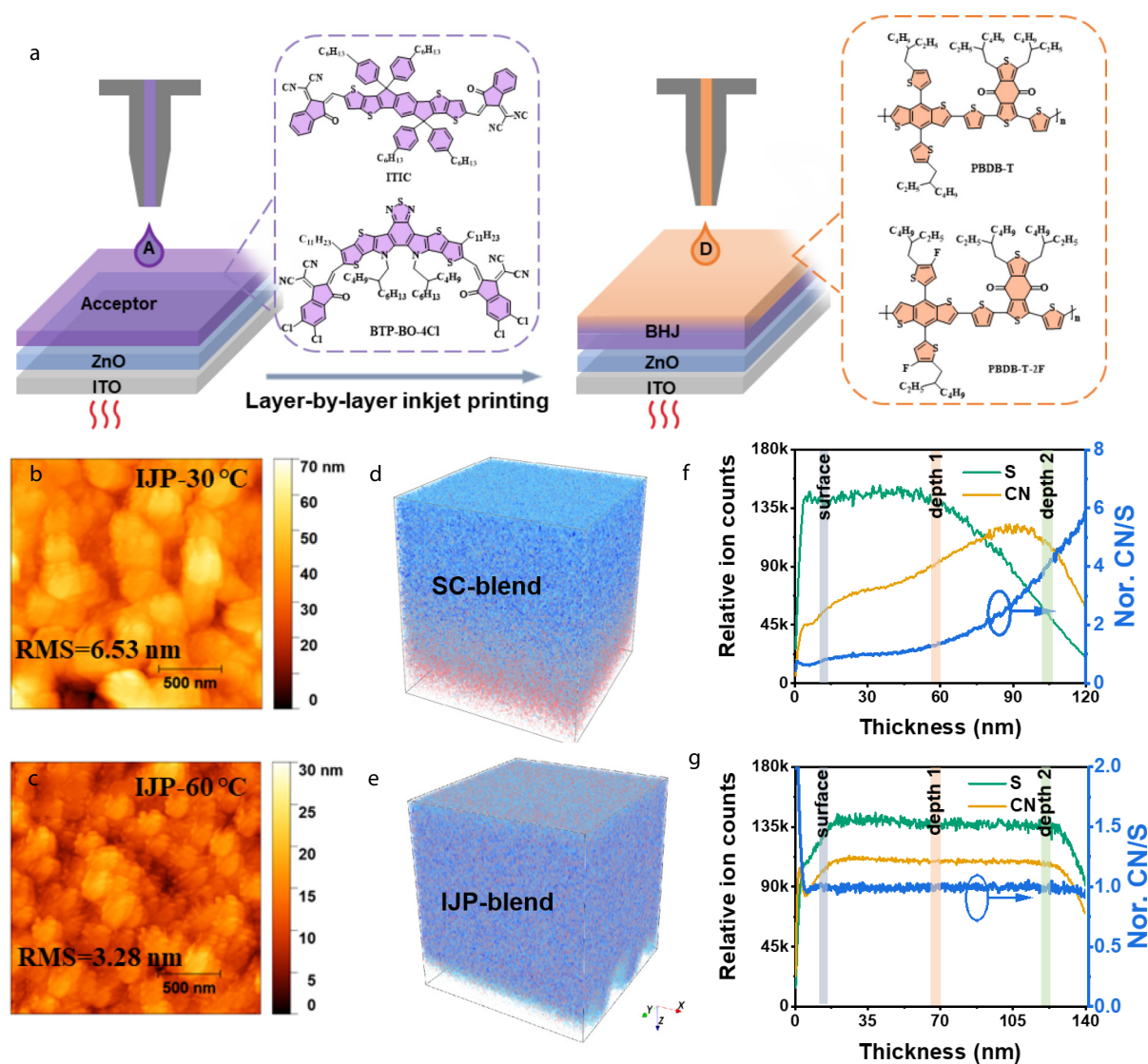
Fig. 19 (a) Diagram illumination of LbL-IJP process and molecular structures of donor and acceptor. (b, c) AFM images of inkjet-printed PBDB-T:ITIC at 30 and 60 °C. ToF-SIMS 3D images (d, e) and curves (f, g) of spin-coated and inkjet-printed PBDB-T:ITIC films, respectively. (Reproduced with permission from Ref. [15]; Copyright (2022) Wiley).

ing of the top electrode, solvent dissolubility is a severe issue that causes inferior performance. In addition, the nozzle is easily blocked by AgNWs, which leads to poor uniformity and low conductivity of the grid electrode.[93] Egelhaaf et al.[49] dispersed AgNWs in high boiling point solvent amyl alcohol to avoid nozzle blockage and successfully prepared the top electrode with a sheet resistance of 20 Ω/□ and transmittance of 94%. As shown in Figs. 20(d) and 20(g), the obtained electrode has good morphology and uniformity, satisfying use both for top and bottom electrodes. Then they found that the transparency (Fig. 20e) and sheet resistance (Fig. 20f) decreased when tuning the printing times from 1 time to 4 times. To gain sufficient conductivity, the semi-transparency electrode was prepared by inkjet printing 4 times. Based on the above results, a performance of 4.3% for 1 cm² semitransparent organic solar cells was obtained. Figs. 20(h) and 20(i) give the J-V curves and EQE of the 1 cm² semitransparency device, respectively.

3.5 Fully Inkjet Printing OSC Devices

As mentioned above, all the functional layers in OSCs, including the front and the back electrodes, the active layer, and the interface layers, have been fabricated by inkjet printing, which implies the great potential of fabricating OSCs through fully inkjet printing. It is also encouraging that different research groups have reported fully printed OSCs with high performance. As a typical example, Kim et al.[94] successfully prepared organic solar cells through fully inkjet printing on the ITO glass substrate by adjusting the deposition parameters of each layer. The optimal printing conditions of ZnO included a substrate temperature of 50 °C and dot spacing of 50 μm. For the active layer, PEDOT:PSS and Ag electrodes, the optimized temperature and drop spacing were 50 °C/50 μm, 30 °C/30 μm, and 80 °C/80 μm, respectively. The device with a structure of glass/ITO/PEDOT:PSS/ P3HT:PCBM/Ag was prepared, and the optimal PCE
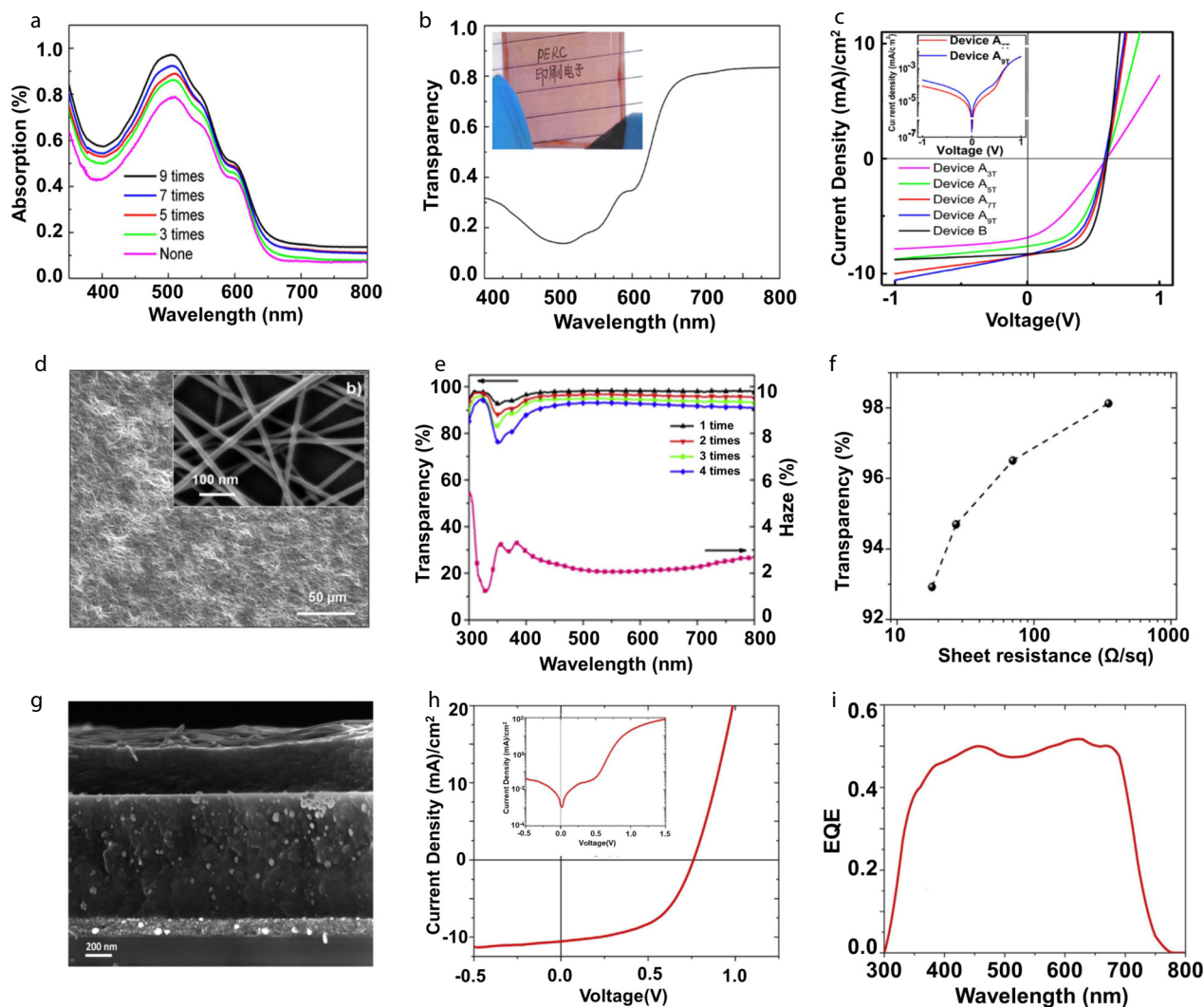
Fig. 20 (a) The absorption of the device before and after printing Ag NW, (b) the transparency of device A7T with the picture in the inset, and (c) typical *J-V* characteristics of the OPV devices with inkjet-printed AgNWs top electrode and thermally deposited Ag top electrode. The inset in (c) shows the comparison of dark *J-V* curves between devices A7T and A9T. (Reproduced with permission from Ref. [92]; Copyright (2015) AIP Publishing). (d) Optical micrograph and SEM image of inkjet-printed AgNWs transparent conductor; (e) Total transmittance of 1−4 times printed AgNWs and haze of 4 times printed AgNWs; (f) Specular transmittance at 550 nm and sheet resistance of inkjet-printed AgNW layers with 1−4 times printing with the glass substrate; (g) Cross-sectional SEM image of the device structure; (h) *J-V* curves of the bright state and the dark state of the inkjet-printed 1 cm^2 device; (i) External quantum efficiency (EQE) of the device. (Reproduced with permission from Ref. [49]; Copyright (2016) Elsevier).

of the device was 1.25%.

Since the metal grid could be used as the front electrode, Groen *et al.*[43] printed all the layers in the devices of Ag-grids/PEDOT:PSS/ZnO/photoactive layer/PEDOT:PSS/Ag. In this work, an industrial printing head containing 512 nozzles that were compatible with R2R (Roll to Roll) process was used. Specifically, Ag-grids were inkjet-printed using a Fujifilm Dimatix Materials Printer (DMP 2831). High conductive PEDOT:PSS (HC-PEDOT:PSS), ZnO nanoparticles, and the photoactive layer were performed on a LP50 printing platform (Pixdro, OTB) using an industrial printhead (KM512LN). With P3HT:PC$_{61}$BM and PV 2000 as organic photoactive layers, they successfully prepared 0.038 cm^2 inkjet-printed devices with efficiencies of 1.7% and 4.1%, respectively.[43] In 2020, Baran *et al.*[44] achieved high efficient full-printed semitransparent

OSCs with an efficiency of 9.5% with a device structure of ITO/ZnO/PTB7-Th:IEICO-4F/PEDOT:PSS nanoparticles/Ag nanoparticles grid. This is an efficiency record of fully inkjet-printed OSCs till now.

As one of the most promising replacements of the HC-PEDOT:PSS and metal grid back electrode, Egelhaaf *et al.*[49] used Ag NWs as both front and back electrodes through inkjet printing, and a fully inkjet-printed semitransparent OSC with 4.3% of 1 cm^2 was reported.

Groen *et al.*[83] also achieved the printing fabrication of large-area modules. Four layers of devices, including HC-PEDOT:PSS modifying layer, ZnO ETL, P3HT:PC$_{61}$BM active layer, and HC-PEDOT:PSS top electrode were printed sequentially. In addition, a mixture of non-halogenated solvents containing *o*-xylene, Indian, and tetraline was utilized in this work

to satisfy the requirement for industrial-scale application. The 92 cm² module gave an efficiency of 0.98%. In the large-area model device, the conventional interconnection between adjacent cells composited three consecutive patterning steps, P1, P2, and P3 as shown in Fig. 21(e). The total area of P1, P2, and P3 is the dead area of modules, which highly influenced the geometric fill factors (GFF) of the module devices. In this architecture, P2 are large visually conspicuous tripes, which would affect the visual appearance. Because of the high printing precision of IJP, Egelhaaf *et al.*[95] developed printing Ag bridges strategy to overcome the problem. The fabrication process is shown in Fig. 21(e). Specifically, they deposited all the functional layers except the top and bottom electrodes through continuous printing. The Ag bridge was inkjet printed on the bottom electrode, which would cross over all the functional layers. The successful fabrication of large-area

OSCs and modules using an industrial printhead demonstrated the feasibility of printing OSCs through R2R high-speed inkjet printing.

Additionally, inkjet printing technology has a high design freedom, which avoids the use of masks during printing patterns. As shown in Fig. 22(a), the Christmas tree device was digitally inkjet-printed. In this device, HC-PEDOT:PSS layer and ZnO ETL fully cover the Ag front electrode (the green region). The photoactive layer was designed restricted in the ETL area at the stem of the tree (the red region). Such a patterned OSC has an effective area of 6.24 cm². Fig. 22(b) shows a printed OSC with an area of 84 cm² with a portrait of Alan J. Heeger.[95] In this work, the device has a structure of ITO/ZnO/P3HT:PC$_{61}$BM/PEDOT:PSS/Ag NWs. A laser patterned P1 and P3 with a width of 0.26 mm and P2 used a printed Ag bridge. On the top of the ITO electrode, ZnO and
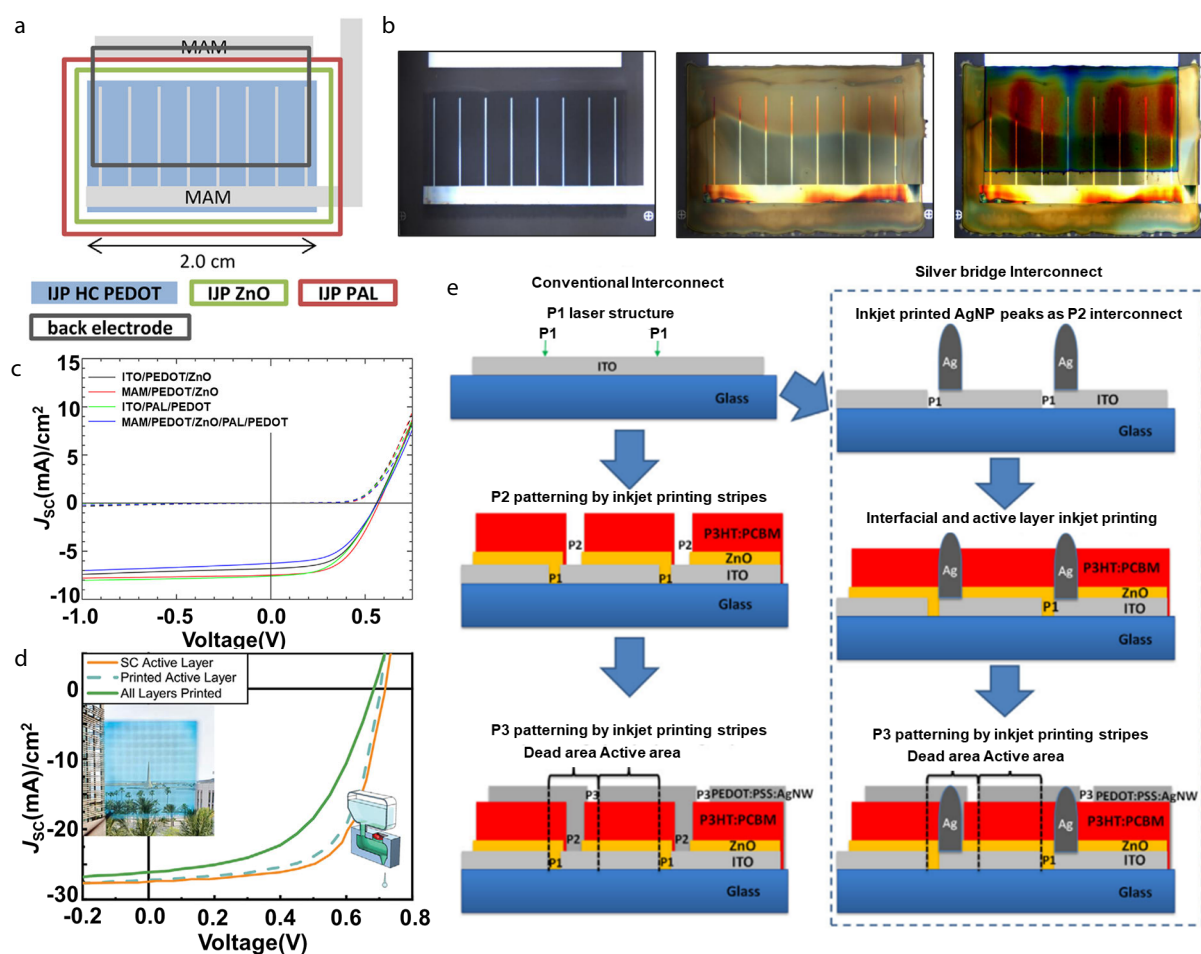

Fig. 21   (a) Schematic illustration of organic solar module fabricated by fully inkjet printing method; (b) Optical micrograph images of OPV cells with multiple inkjets printed layers: (left) PEDOT and ZnO, (middle) PEDOT/ZnO and photoactive layer, and (right) PEDOT/ZnO/P3HT:PC$_{61}$BM and PEDOT, printing direction is from bottom to top; (c) The *J-V* characteristics of the 92 cm² inkjet-printed OSCs module. *J-V* characteristics of the full inkjet-printed semitransparent OSCs. (Reproduced with permission from Ref. [83]; Copyright (2015) Elsevier). (d) *J-V* curves of the coated and printed devices and an image of a semitransparent fully printed device. (Reproduced with permission from Ref. [44]; Copyright (2020) Wiley). (e) In conventional gap layout, interconnection is achieved by introducing a gap during the active and interlayer printing process so that the top electrode can diffuse into the gap and form a connection with the bottom electrode. The novel bridge interconnects proposed in this work is highlighted in a blue dashed bracket. AgNP peaks are printed so that the top and bottom electrodes can be bridged at the interconnection area. (Reproduced with permission from Ref. [95]; Copyright (2018) Wiley).

P3HT:PC$_{61}$BM layer were sequentially deposited by inkjet printing, and PEDOT:PSS and AgNWs were also fabricated through inkjet printing. Around 5% of the blank remained to avoid the overlap of top and bottom electrodes. All the single devices were designed to have the same area. This module gave a performance of 1.6% with a V_{OC} of 5.5 V, a J_{SC} of 6.8 mA/cm^2, FF of 47%, and GFF of 95%.

Inkjet printing technology can not only realize patternable device preparation but also fabricate device arrays in a large area and multi-scale. Alalawe *et al*. used an industrial printing platform to prepare 1500 device arrays containing different sizes on polyethylene naphthalate (PEN) flexible substrate, as shown in Fig. 22(c). The device arrays with different areas of 5, 7.5, 10, 12.5, 17.5 and 20 mm^2 were fabricated, and commercially available electronic inks were used. By optimizing printing parameters, the device array reached a PCE of 0.18% and

the fabrication yield exceeded 70%. As a typical additive manufacturing technology, inkjet printing has the advantage of multi-substrate compatibility. Baran *et al*. successfully realized the fully inkjet printing of OSC on the 1.7 μm ultra-thin polyparaxylene film and ordinary glass, and the device efficiency reached 3.6% and 4.73%, respectively. Previously, ultrathin organic solar cells are mainly prepared on ultrathin substrates by spin-coating or thermal evaporation techniques, but the device geometry, design freedom, and feasibility are greatly limited in the preparation process. As a contactless printing technology, inkjet printing has certain advantages in preparing ultra-thin devices. As reported by Baran *et al*., the ultrathin device used cross-linked PEDOT:PSS as an electrode (Fig. 22d). Such an ultrathin device was stable after being exposed to water for 6 h. Fig. 22(e) was the device structure of ultra-thin organic solar cells, the photographs of
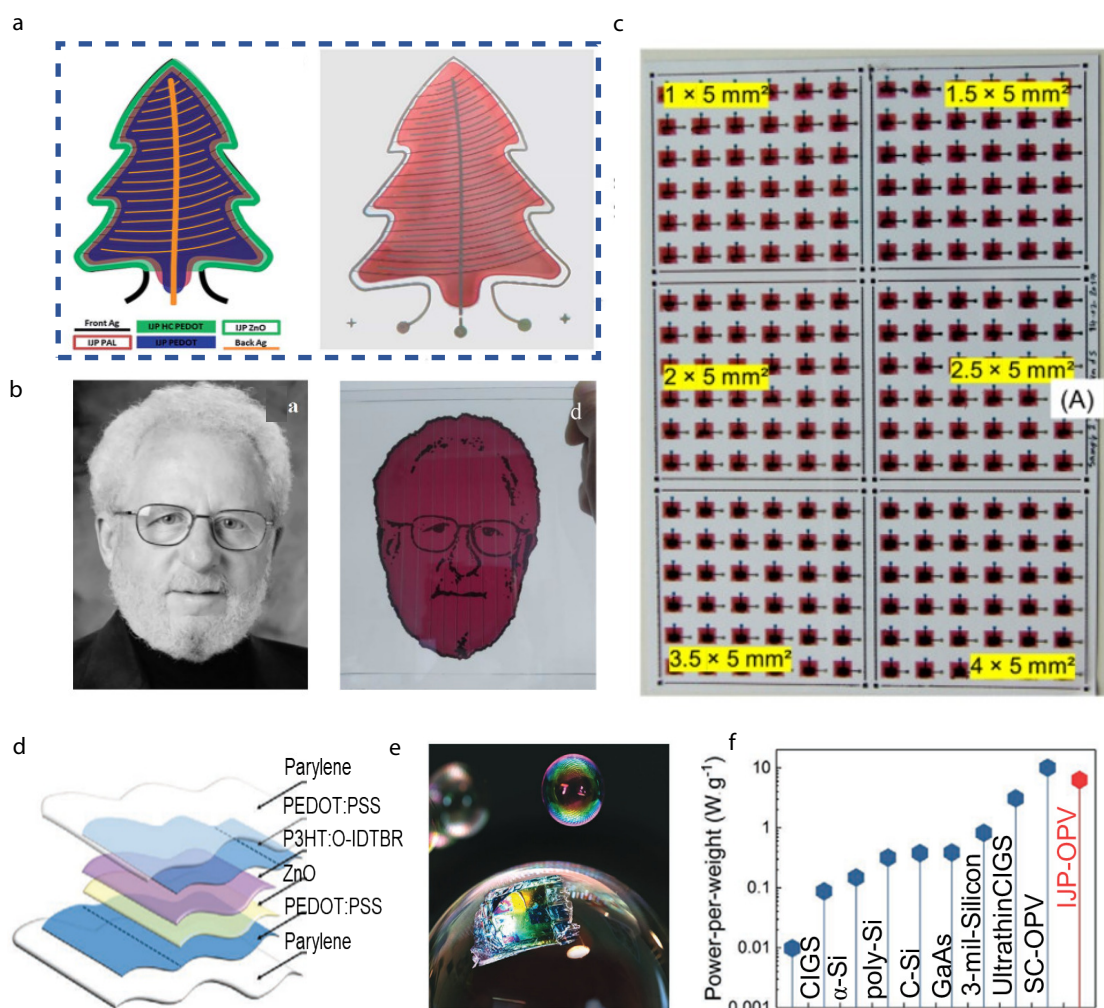
Fig. 22   (a) Organic solar cell in the shape of a Christmas tree, left: schematic representation of printed layers layout, right: photograph of finished fully inkjet-printed OSCs Christmas tree. (Reproduced with permission from Ref. [43]; Copyright (2015) The Royal Society of Chemistry). (b) Photo (left) and the completed OPV-M portrait (right) of Alan Heeger. (Reproduced with permission from Ref. [95]; Copyright (2018) Wiley-VCH). (c) Photograph showing OSCs array with all six active areas printed, 5, 7.5, 10, 12.5, 17.5 and 20 mm^2. (Reproduced with permission from Ref. [96]; Copyright (2018) MDPI). (d) Schematic of the layer-by-layer composition of the solar cells; (e) Photograph of the formation of ultralight inkjet-printed organic solar cells embedded in a soap bubble; (f) Comparison of the power-per-weight values of different cell compositions and the printed OSCs. (Reproduced with permission from Ref. [97]; Copyright (2020) Wiley).

the device on a bubble, and (Fig. 22f) the power-per-weight values compared with the references. Table 4 listed the performance of fully IJP OSCs.

4 DEVELOPMENT OF INKJET-PRINTED PEROVSKITE SOLAR CELLS

Over the past 10 years, the PCEs of perovskite solar cells (PVSCs) have increased from 3.8% to 25.5%, exhibiting great application prospects. However, the high-performance PVSCs were mainly fabricated by spin coating with an area of <0.1 cm², limiting on the laboratory scale. With the development of the inkjet printing technology, many efforts were also made to develop the inkjet printing of PVSCs. Fig. 23 shows the development of the IJP PVSCs. In 2014, Yang et al.[99] firstly fabricated the planar carbon electrode-based perovskite solar cells by inkjet printing perovskite layer and nanocarbon electrode, and obtained a PCE of 11.6%. They inkjet printed carbon ink on top of the PbI_2 layer and then immersed it into a MAI solution to obtain the final device. In 2015, Song and co-workers[100] successfully employed IJP to fabricate a $MAPbI_3$ perovskite film on mesoporous TiO_2, and obtained a PCE of 12.3%. In 2019, Eggers et al.[16] inkjet-printed triple-cation perovskite layers with exceptional

thicknesses of >1 μm, and obtained the highest PCE of 21.6%. In 2022, Chalkias et al.[101] reduced the coffee-ring defects by regulating the concentration of the precursor, and achieved performance of 10.85% and 9.09% on fully printed perovskite small-area (0.34 cm²) device and submodule (34.2 cm²), respectively. In the following part, we will introduce the development of inkjet printing PVSCs in the aspects of ink engineering and the printing process.

4.1 Ink Engineering

The precursor materials and solvents have a significant impact on the film formation process and film quality. Optimizing the composition of the ink with appropriate additives is an effective strategy to improve the morphology of inkjet-printed perovskite films. For instance, Gheno et al.[102] investigated the wettability behavior of different ink fractions on the substrate to produce homogenous perovskite layers by inkjet printing. The Owens-Wendt-Rabel-Kaelble (OWRK) model is applied to investigate the effects of chloride, bromide, and diiodooctane on the wetting property during the inkjet-printing process. The use of chlorine or bromine tended to increase the wettability of perovskite inks, leading to better impregnation of the ink into the rough materials. The improved wettability was likely to be related to the nucleation process of perovskite crystallites in the

Table 4 Photoelectric properties of fully inkjet-printed organic solar cells in literature.

| Device structure	Area (cm²)	V_{OC} (V)	J_{SC} (mA/cm²)	FF (%)	PCE (%)	Machine
glass/Ag/PEDOT:PSS/ZnO/PV2000/PEDOT/Ag-grid	1	0.77	10.4	51	4.1	DMP 2831 [43]
glass/ITO/ZnO/P3HT:PCBM/PEDOT:PSS/Ag	0.1	0.6	6.02	35	1.25	Omijet100 [94]
glass/Ag/ZnO/P3HT:PCBM/PEDOT:PSS/Ag-grid	0.25	0.564	7.11	62.6	2.5	DMP 2800 [98]
PET/Ag/ZnO/P3HT:PCBM/PEDOT:PSS/Ag	0.2	0.42	0.28	34	0.18	KM512LN [96]
glass/Ag/PEDOT/ZnO/P3HT:PCBM/PEDOT:PSS/Ag-grid	0.1	0.71	10.39	64.64	4.73	DMP 2800 [97]
glass/ITO/ZnO/PTB7-Th:IEICO-4F /PEDOT:PSS/Ag	0.1	0.69	26.1	53.2	9.24	DMP 2800 [44]
AgNWs/ZnO/PV2000/PC₇₁BM/PEDOT:PSS/AgNWs	1	0.76	10.7	52.8	4.3	KM512LN [83]
ITO/PEDOT:PSS/PCDTBT:PC₇₁BM/ZnO/Ag	0.5	0.89	9.95	56.78	5.05	DMP 2831 [37]
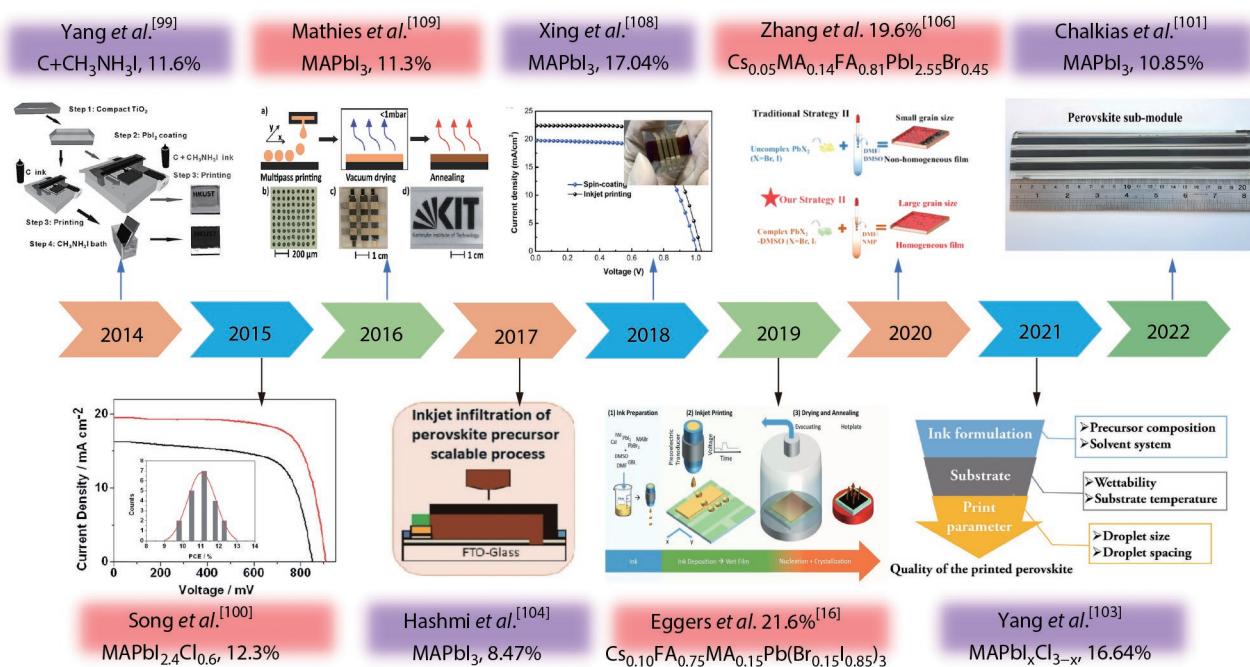
Fig. 23 Efficiency development of the inkjet-printed perovskite solar cells.

presence of chlorine. In contrast, the diiodooctane did not seem to affect the wettability. Finally, an efficiency of 10.7% was obtained for the fully inkjet-printed perovskite solar cell. Xu *et al*.[103] studied the effects of precursor composition on the morphology and microstructure of the printed perovskite films during the heat-assisted inkjet-printing process. They found that the plate-like crystals were obtained when pure lead acetate (PbAc$_2$) was used as the precursor (Fig. 24a), which has been due to its fast crystallization speed. The introduction of lead chloride (PbI$_2$) in the precursor led to the formation of homogenous crystals, which was due to the suppression of excessive rapid crystallization. Consequently, a champion PCE of 16.6% was obtained for the inkjet-printed devices by optimizing the content of the PbAc$_2$ based on the MAPbI$_x$Cl$_{3-x}$ photoactive layer.

Apart from manipulating the precursor materials, additives were also effective to regulate the crystallization speed and improve the uniformity of the inkjet-printed perovskite films. In 2017, Hashmi *et al*.[104] utilized 5-ammonium valeric acid iodide (5-AVAI) as ink additives and found 5-AVAI could slow down the perovskite crystal growth, thereby improved crystalline network was obtained, which enabled the achievement of efficiency of 8.47% for the carbon electrode-based perovskite solar cells. Pathak *et al*.[105] found that the polymer additive, like PTB7 also can modify the crystallization dynamics of film formation and improve the quality. Devices with PTB7 additives pushed the improvement of PCE from 8.0% to 10.35% compared to the device without additives.

During the film formation process of perovskite, the nucleation and crystallization are accompanied by the evaporation of the solvent. Choosing the proper solvent with wide printability and solubility is the key to realizing high-efficiency PVSCs devices. During the inkjet printing of perovskite, the faster crystallization of perovskite leads to the formation of roughness films and more defects. Therefore, the basic requirement of solvent selection is to make sure reasonable crystallization speed to ensure high-quality films. Li *et al*.[106] chose a mixture of methyl pyrrolidone (NMP) and dimethyl

formamide (DMF) as the solvent to form the PbX$_2$-DMSO (X=Br, I) precursor solution. (Fig. 24b), which effectively slowed down the crystallization rate of perovskite during the printing process. The printed Cs$_{0.05}$MA$_{0.14}$FA$_{0.81}$PbI$_{2.55}$Br$_{0.45}$ perovskite film exhibited grain size around 500 nm and low roughness. Finally, an efficiency of 19.6 % was achieved in the 0.04 cm^2 device, and 89% of the initial efficiency was maintained after degradation for 1000 h in air with humidity less than 20%. During the printing process, though several kinds of solvents have been developed and worked well. However, the development of nontoxic green alternative solvent systems is rarely reported and is highly desirable. In 2021, Wojciechowski *et al*.[107] added a green additive into the precursor solution to promote perovskite crystallization during the printing process. A highly coordinated Lewis base additive, thiosemicarbazide (TSC) was used, and a stable intermediate phase PbI$_2$/TSC$_x$ was obtained (Fig. 24c). Consequently, an efficiency of 11.4% was obtained for the 1 cm^2 device.

4.2 Printing Engineering

During inkjet printing, substrate character and substrate temperature have a profound impact on the films quality of perovskite. Xing *et al*.[108] tailored the surface wettability using fullerene (C$_{60}$) modifying modified TiO$_2$. They found less dense nuclei and larger grain sizes (Fig. 25a) were obtained when the substrate has an appropriate wettability. Meanwhile, C$_{60}$ also can reduce hysteresis owing to its high electron mobility. Finally, a PCE of 17.04% (0.04 cm^2) and 13.27% (4 cm^2) was achieved *via* one-step inkjet printing. Eggers *et al*.[16] investigated the effects of the ink composition, surface treatment, and annealing methods on the IJP perovskite films. Oxygen plasma was used to treat the NiO$_x$ surface, which avoided the formation of holes in the wet film. Meanwhile, they increased the film thickness (400 nm to 4 μm) by increasing the printing resolution (600–2000 dpi) (Fig. 25b). It was found that with increasing printing resolution and thickness, the perovskite film crystals grew in a columnar pattern and exhibited a lower defect density. Finally, with optimized printing parameters, high-
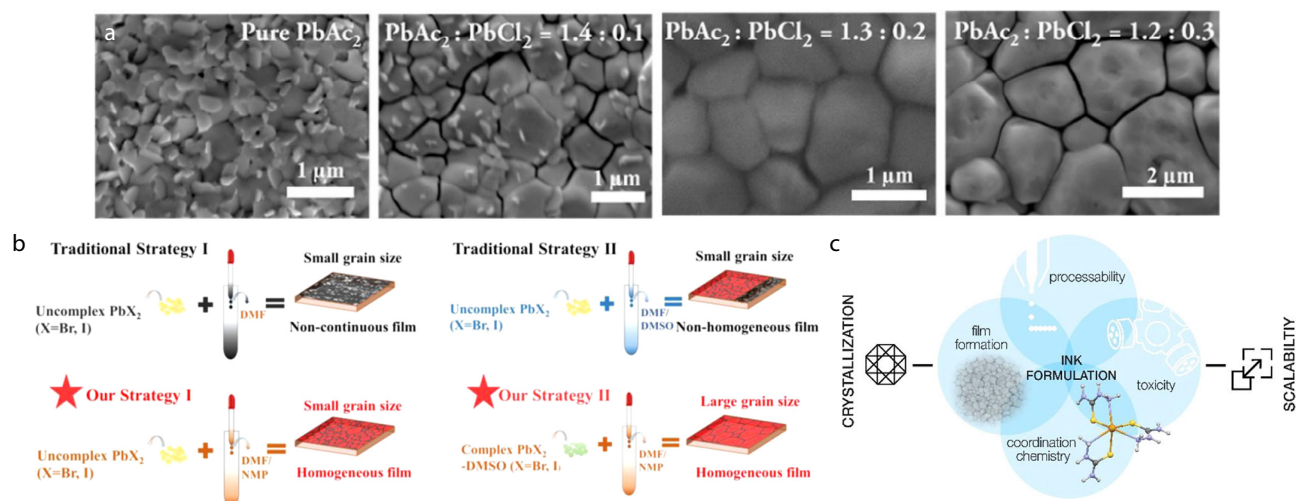
Fig. 24   (a) SEM images of ambient printed perovskite films using different precursor compositions. (Reproduced with permission from Ref. [103]; Copyright (2021) Wiley-VCH). (b) Schematic diagram of different ink engineering of inkjet-printed perovskite films. (Reproduced with permission from Ref. [106]; Copyright (2020) American Chemical Society). (c) Green solvent-based perovskite precursor development for inkjet-printed flexible solar cells. (Reproduced with permission from Ref. [107]; Copyright (2021) American Chemical Society).

quality inkjet-printed triple-cation perovskite layers with exceptional thicknesses of >1 μm are obtained, which enabled encouragingly high PCEs of 21.6% and stabilized power output efficiencies of 18% for inkjet-printed PVSCs.

Besides surface treatment, substrate temperature and printing drop spacing are also important for inkjet printing PSC films. Li et al.[100] investigated the effects of substrate temperature on inkjet-printed perovskite films. It was found that the films printed at 25 °C contained un-homogenous films with different shapes When the temperature was increased from 40 °C to 60 °C, more round and flattened crystals appeared, and the crystal size further increased, but a large number of pinholes were formed on the surface, which was unfavorable for the photovoltaic performance of the device. Based on this, the highest PCE of 12.3% was obtained with high reproducibility. In 2016, Mathies et al.[109] investigated the effect of printing drop spacing on the performance of the perovskite device. Vacuum annealing was developed to obtain uniform and smooth films. Subsequently, the PCEs of inkjet-printed devices increased from 4.4% to 11.3 % with the increase in printing times at a drop spacing of 45 μm. Nazeeruddin et al.[110] optimized the printing temperatures and drop spacing to regulate the thickness and morphology of the PSC layer, and realized a 14.11% PCE based on an inkjet-printed mesoporous TiO_2 and perovskite layer.

As a typical "sandwich" structure for the perovskite solar cell, the film quality of the perovskite films highly depended on the wettability between the buffer layer and inks. Therefore, the surface energy of the buffer layer played an important role in the crystallization and growth process. Schackmar et al.[111] selected NiO_x and PCBM as HTL and ETL to prepare

devices with $ITO/NiO_x/Cs_{0.10}FA_{0.75}MA_{0.15}Pb(Br_{0.15}I_{0.85})_3/$ PCBM/BCP/Au structures. In this work, they first used oxygen plasma to treat ITO for printing NiO_x and obtained homogenous films. And then isopropanol was used to treat the NiO_x layer for reducing surface energy to enable the inkjet printing of the perovskite absorber layer. By systematically optimizing the printing parameters interfacial layer and annealing temperatures, the highest great efficiency of 17.2% was obtained based on a fully inkjet-printed device. In addition, precursor regulation is also effective to regulate the wettability between inks and the substrates. Chalkias et al.[101] regulated the concentration of the precursor to reduce the coffee-ring defects, leading to improved film quality and higher efficiency, and more stable photovoltaic devices. Consequently, fully printed perovskite small-area devices and submodules with 34.2 cm² and solar cells exhibited performances of 10.85% and 9.09% (Fig. 25c), respectively.

Regarding the future application of the perovskite solar cells, the colors and shapes design also needs to be taken into account. In particular, for the application of integrated building photovoltaics, the color of dark-colored PV is still a drawback. Schlisske et al.[112] prepared a colorized device by combining a luminescent layer of dye and a perovskite layer, taking advantage of the high freedom of inkjet printing. The luminescent down-shifting (LDS) layer was inkjet-printed on the back of the glass, and then the perovskite device was prepared on the front of the glass through inkjet printing. The device efficiency of the PVSC decreased moderately from 11.5% to 9.4% due to the absorption generated by the luminescent layer but showed very strong coloring on the dark perovskite (Fig. 25d). This work facilitated the advancement of
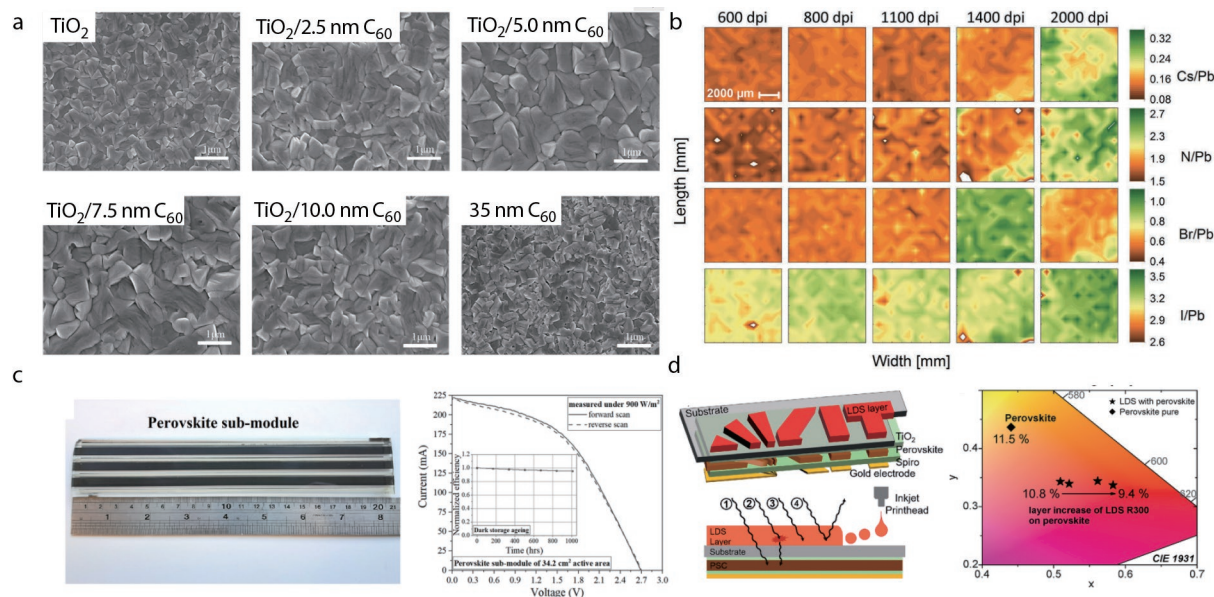
Fig. 25   (a) SEM images of inkjet printed $MAPbI_3$ films on TiO_2, TiO_2/2.5 nm C_{60}, TiO_2/5.0 nm C_{60}, TiO_2/7.5 nm C_{60}, TiO_2/10.0 nm C_{60}, and 35nm C_{60}. (Reproduced with permission from Ref. [108]; Copyright (2018) Wiley-VCH). (b) XPS (X-ray photoemission spectroscopy) mapping of perovskite inkjet printed with different printing resolutions. The mapping area is 8 mm × 8 mm for each sample. Four elemental ratios (Cs/Pb, N/Pb, Br/Pb, and I/Pb) are shown in the rows. (Reproduced with permission from Ref. [16]; Copyright (2020) Wiley). (c) Image of the fully-printed perovskite submodule of 34.2 cm² active area and *J-V* curve. (Reproduced with permission from Ref. [101]; Copyright (2022) Wiley). (d) The left part is the structure of the device, and the right part is CIE 1931 diagram with the color perceptions of PSCs. (Reproduced with permission from Ref. [112]; Copyright (2019) American Chemical Society).

Table 5   Photoelectric properties of inkjet printed perovskite solar cells.

Materials	Solvent system (V:V)	Area (cm^2)	V_{OC} (V)	J_{SC} (mA·cm^{-2})	FF (%)	PCE (%)	Machine
C+CH$_3$NH$_3$I	isopropanol	0.15	0.95	17.20	71	11.6	Cannon IP188 [99]
CH$_3$NH$_3$PbI$_{3-x}$Cl$_x$	DMF	—	0.74	22.1	65	10.7	DMP 2850 [102]
MAPbI$_x$Cl$_{3-x}$	DMF	0.1	0.95	22.28	78.6	16.64	MicroFab [103]
MAPbI$_3$	GBL:5-VAVI	0.16	0.84	15.3	65.7	8.47	DMP 2831 [104]
Cs$_{0.05}$FA$_{0.79}$MA$_{0.16}$Pb(Br$_{0.17}$I$_{0.83}$)$_3$	GBL	0.16	1.07	20.18	48.0	10.35	PixDro LP50 [105]
Cs$_{0.05}$MA$_{0.14}$FA$_{0.81}$PbI$_{2.55}$Br$_{0.45}$	NMP/DMF (1:1)	0.04	1.11	23.48	76.2	19.6	DMP 2831 [106]
Cs$_{0.1}$[(HC(NH$_2$)$_2$)$_{0.83}$(CH$_3$NH$_3$)$_{0.17}$]$_{0.9}$Pb(I$_{0.83}$Br$_{0.17}$)$_3$	GBL/2MP/ DMSO (9.5:4.15:1)	1	1.00	19.00	69.2	11.4	PixDro LP50 [107]
MAPbI$_3$	DMSO:GBL (4:6)	0.04	1.08	22.71	69.6	17.04	DMP 2831 [108]
		4	1.04	20.40	62.6	13.27	
Cs$_{0.10}$FA$_{0.75}$MA$_{0.15}$Pb(Br$_{0.15}$I$_{0.85}$)$_3$	DMF:DMSO:GBL(28:26:46)	0.105	1.11	24.6	80	21.6	PixDro LP50 [16]
MAPbI$_{2.4}$Cl$_{0.6}$	GBL	0.04	0.91	19.55	69	12.3	DMP 2831 [100]
MAPbI$_3$	GBL:DMSO (7:3)	0.09	1.00	18.4	56	11.3	DMP 2800 [109]
Cs$_{0.10}$Gua$_{0.05}$FA$_{0.83}$MA$_{0.17}$PbI$_{2.63}$Br$_{0.37}$	DMF:DMSO:GBL:NMP (33:28:33:5)	0.064	1.01	16.19	68.2	14.11	DMP 2850 [110]
Cs$_{0.10}$FA$_{0.75}$MA$_{0.15}$Pb(Br$_{0.15}$I$_{0.85}$)$_3$	DMF:DMSO:GBL(28:26:46)	0.105	1.02	23.6	71.5	17.2	DMC-16610 [111]
		1	1.02	18.8	64	12.3	
MAPbI$_3$	DMF	0.34	0.93	22.03	53	10.85	DMP 2850 [101]
		34.2	0.89	19.47	47	9.09	
Cs$_{0.10}$(FA$_{0.83}$MA$_{0.17}$)$_{0.9}$Pb(Br$_{0.17}$I$_{0.83}$)$_3$	DMF:DMSO:GBL(26:28:46)	0.09	1.06	21.5	67	9.4	DMP [112]

building PV integration and also extended the application of inkjet-printed PSCs. Table 5 lists the performance of the PVSCs in the literature.

5 PERSPECTIVE

Since the first report of inkjet-printed OSCs in 2007, many efforts have been devoted to solving several fundamental problems, including ink formation, coffee ring control, and morphology manipulation (as summarized in Fig. 26). Therefore, significant developments in IJP OSCs and PVSCs were achieved with the highest performance of 13.09% and 21.6%, respectively. However, this is still a big gap between the efficiency of IJP solar cells and spin-coated devices. Take the OSCs for instance, there are two main reasons for the low efficiency. Firstly, low boiling points solvents such as chloroform and chlorobenzene are the most commonly used solvents for highly efficient OSCs during spin-coating. However, in the case of inkjet printing, nozzles would be clogged if using low boiling point solvents. On the other hand, most current photoactive materials have poor solubility in high boiling point solvents, such as *o*-dichlorobenzene, resulting in a large phase separation of the BHJ film morphology. Due to these challenges, the inkjet-printed non-fullerene OSCs are not sufficiently developed. Based on the high performance of inkjet-printed devices and the unique advantages of patternable and materials-saving, we can predicate its future application of IJP in large-area OSCs and PVSCs.

However, there is still a big gap between the efficiency of the inkjet-printed OSCs and the devices prepared by spin-coating, doctor-blade coating, and slot-die coating. The following two aspects might be the main problems.

First, the basic challenge originated from the inks: it has the highest requirement of rheology property for the inks for IJP than other coating and printing technologies. Several studies have demonstrated using high boiling point solvent or non-halogen solvent in IJP resulted in inferior device performance due to unfavorable morphology, which will be a big obstacle for performance enhancement. We could find that inkjet-printed organic photoactive materials could be divided into two categories. The initial investigated organic active layer could give comparable or even higher performance through inkjet printing than the coating method. That is because these materials need relatively large and oriented crystallites, thereby printing slow drying is suitable to fabricate these devices. However, recent works reported that non-fullerene system would generally form excessive molecular aggregates as fabricated from high-boiling point solvent. Most of the early work focuses on optimizing the printing parameters, such as printing dot space, substrate, and ink temperature. High-temperature printing is possible to improve the device performance. However, new issues, such as nozzle blocking or unfavorable droplet coalesce would be formed through substrate or nozzle heating treatment. Given these difficulties, the printed device still gave much lower performance than the coated devices. The encouraging thing is additive and ternary engineering have been widely used and proved effective to regulate the nanomorphology of the organic active layer in the coating method, thereby it should be the potential to achieve ideal nano-morphology through similar strategies in the case of inkjet-printing. Therefore, ink formulation is the root of all the problems, more attention should be paid to ink engineering through additive and ternary strategies in the future.

Second, the large-scale application of inkjet printing technology in organic solar cells is challenged due to more difficulties in controlling the nozzle block and satellite and regulating the morphology of the blend films. Concerning the full-printed devices, the ink formulation should have suitable rheological properties and proper interface compatibility, and interface wettability to ensure the formation of surface films with excellent charge transport. In addition, though several works have reported that inkjet-printed OSCs from non-halogen solvent, it is still not an environmental-friendly process. Green solvent printing should be the ultimate goal of inkjet printing. Regarding these, water/ethanol-dispersed organic
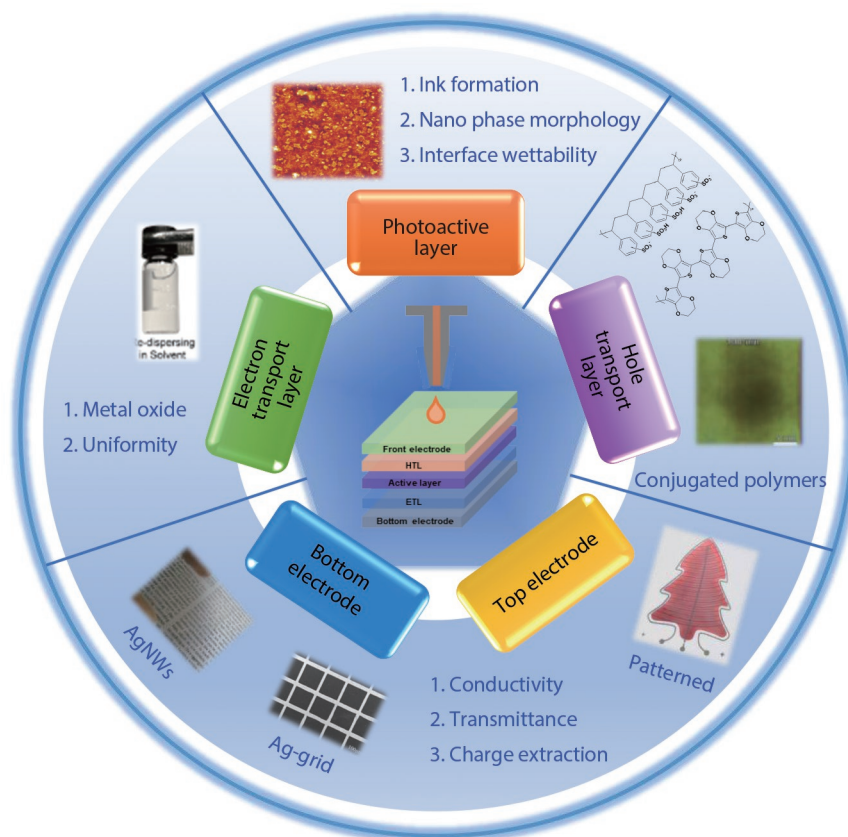
Fig. 26   Summary of the development of the inkjet-printed organic solar cells.

semiconductor nanoparticles through the surfactants route using proper surfactants[113,114] have been developed. In addition, p-doping agent 2,3,5,6-tetrafluoro-7,7,7,8-tetracyanoquinodimethane (F4TCNQ) could help the organic materials P3HT and P3HT: ICBA to disperse in ethanol solvent.[115] It seems that such a nanoparticle strategy might be a feasible solution method to inkjet-print these nanoparticles and achieve the green printing of OSCs. Besides, developing new materials that could be fabricated from green solvents is another solution. However, the device from both the organic nanoparticles route and the new materials routes still gave low device performance, thereby it still has a long way to go to achieve green printing.

BIOGRAPHIES

Qun Luo received her Ph.D. form Zhejiang University in 2011. Then she worked as a postdoc at Suzhou Institute of Nano-Tech and Nano-Bionics, CAS. Currently she is a professor at Suzhou Institute of Nano-Tech and Nano-Bionics. Her research interests include printable materials and interface engineering in flexible and large-area printed solar cells.

Chang-Qi Ma received his Ph.D. at the Technical Institute of Physics and Chemistry, CAS. After that, he worked as a postdoc at Heriot-Watt University (UK), and then he joined University of Ulm in 2004 as a Humboldt fellow. From January 2007 to May 2011, he did his Habilitation at Institute of Organic Chemistry II and Advanced Materials, Ulm University. In June 2011, he joined Suzhou Institute of Nano-Tech and Nano-Bionics, CAS as a professor. His research focuses on printing processing and stability of organic solar cells.

Conflict of Interests

The authors declare no interest conflict.

ACKNOWLEDGMENTS

REFERENCES

1   Ameri, T.; Khoram, P.; Min, J.; Brabec, C. J. Organic ternary solar cells: A review. *Adv. Mater.* **2013**, *25*, 4245−4266.

2   Hou, J.; Inganas, O.; Friend, R. H.; Gao, F. Organic solar cells based on non-fullerene acceptors. *Nat. Mater.* **2018**, *17*, 119−128.

3   Zhang, J.; Tan, H. S.; Guo, X.; Facchetti, A.; Yan, H. Material insights and challenges for non-fullerene organic solar cells based on small molecular acceptors. *Nat. Energy* **2018**, *3*, 720−731.

4   Fukuda, K.; Yu, K.; Someya, T. The future of flexible organic solar cells. *Adv. Energy Mater.* **2020**, *10*, 2000765.

5   Kearns, D.; Calvin, M. Photovoltaic effect and photoconductivity

in laminated organic systems. *J. Phys. Chem. Lett.* **1958**, *29*, 950–951.

6 Tang, C. W. Two-layer organic photovoltaic cell. *Appl. Phys. Lett.* **1986**, *48*, 183–185.

7 Yu, G.; Gao, J.; Hummelen, J. C.; Wudl, F.; Heeger, A. J. Polymer photovoltaic cells: enhanced efficiencies *via* a network of internal donor-acceptor heterojunctions. *Science* **1995**, *270*, 1789–1791.

8 Cui, Y.; Xu, Y.; Yao, H.; Bi, P.; Hong, L.; Zhang, J.; Zu, Y.; Zhang, T.; Qin, J.; Ren, J.; Chen, Z.; He, C.; Hao, X.; Wei, Z.; Hou, J. Single-junction organic photovoltaic cell with 19% efficiency. *Adv. Mater.* **2021**, *33*, 2102420.

9 Bi, P.; Zhang, S.; Ren, J.; Chen, Z.; Zheng, Z.; Cui, Y.; Wang, J.; Wang, S.; Zhang, T.; Li, J.; Xu, Y.; Qin, J.; An, C.; Ma, W.; Hao, X.; Hou, J. A high-performance nonfused wide-bandgap acceptor for versatile photovoltaic applications. *Adv. Mater.* **2022**, *34*, 2108090.

10 Kojima, A.; Teshima, K.; Shirai, Y.; Miyasaka, T. Organometal halide perovskites as visible-light sensitizers for photovoltaic cells. *J. Am. Chem. Soc.* **2009**, *131*, 6050–6051.

11 Kim, H. S.; Lee, C. R.; Im, J. H.; Lee, K. B.; Moehl, T.; Marchioro, A.; Moon, S. J.; Humphry-Baker, R.; Yum, J. H.; Moser, J. E.; Gratzel, M.; Park, N. G. Lead iodide perovskite sensitized all-solid-state submicron thin film mesoscopic solar cell with efficiency exceeding 9%. *Sci. Rep.* **2012**, *2*, 591.

12 Jiang, Q.; Zhao, Y.; Zhang, X.; Yang, X.; Chen, Y.; Chu, Z.; Ye, Q.; Li, X.; Yin, Z.; You, J. Surface passivation of perovskite film for efficient solar cells. *Nat. Photon.* **2019**, *13*, 460–466.

13 Peng, J.; Kremer, F.; Walter, D.; Wu, Y.; Ji, Y.; Xiang, J.; Liu, W.; Duong, T.; Shen, H.; Lu, T.; Brink, F.; Zhong, D.; Li, L.; Lee Cheong Lem, O.; Liu, Y.; Weber, K. J.; White, T. P.; Catchpole, K. R. Centimetre-scale perovskite solar cells with fill factors of more than 86 per cent. *Nature* **2022**, *601*, 573–578.

14 Yoo, J. J.; Seo, G.; Chua, M. R.; Park, T. G.; Lu, Y.; Rotermund, F.; Kim, Y. K.; Moon, C. S.; Jeon, N. J.; Correa-Baena, J. P.; Bulović, V.; Shin, S. S.; Bawendi, M. G.; Seo, J. Efficient perovskite solar cells *via* improved carrier management. *Nature* **2021**, *590*, 587–593.

15 Chen, X.; Huang, R.; Han, Y.; Zha, W.; Fang, J.; Lin, J.; Luo, Q.; Chen, Z.; Ma, C. Q. Balancing the molecular aggregation and vertical phase separation in the polymer: Nonfullerene blend films enables 13.09% efficiency of organic solar cells with inkjet-printed active layer. *Adv. Energy Mater.* **2022**, *12*, 2200044.

16 Eggers, H.; Schackmar, F.; Abzieher, T.; Sun, Q.; Lemmer, U.; Vaynzof, Y.; Richards, B. S.; Hernandez-Sosa, G.; Paetzold, U.W. Inkjet-printed micrometer-thick perovskite solar cells with large columnar grains. *Adv. Energy Mater.* **2020**, *10*, 1903184.

17 Yang, X.; Lin, Y.; Wu, T.; Yan, Z.; Chen, Z.; Kuo, H. C.; Zhang, R. An overview on the principle of inkjet printing technique and its application in micro-display for augmented/virtual realities. *Opto-Electr. Adv.* **2022**, *5*, 210123–210123.

18 Sawa, M.; Fantuzzi, A.; Bombelli, P.; Howe, C. J.; Hellgardt, K.; Nixon, P. J. Electricity generation from digitally printed cyanobacteria. *Nat. Commun.* **2017**, *8*, 1327.

19 Han, G. D.; Bae, K.; Kang, E. H.; Choi, H. J.; Shim, J. H. Inkjet printing for manufacturing solid oxide fuel cells. *ACS Energy Lett.* **2020**, *5*, 1586–1592.

20 Sandler, N.; Maattanen, A.; Ihalainen, P.; Kronberg, L.; Meierjohann, A.; Viitala, T.; Peltonen, J. Inkjet printing of drug substances and use of porous substrates-towards individualized dosing. *J. Pharm. Sci.* **2011**, *100*, 3386–3395.

21 Karunakaran, S. K.; Arumugam, G. M.; Yang, W.; Ge, S.; Khan, S. N.; Lin, X.; Yang, G. Recent progress in inkjet-printed solar cells. *J. Mater. Chem. A* **2019**, *7*, 13873–13902.

22 Ganesan, S.; Mehta, S.; Gupta, D. Fully printed organic solar cells-a review of techniques, challenges and their solutions.

Opto-Electron. Rev. **2019**, *27*, 298–320.

23 Daly, R.; Harrington, T. S.; Martin, G. D.; Hutchings, I. M. Inkjet printing for pharmaceutics—a review of research and manufacturing. *Int. J. Pharm.* **2015**, *494*, 554–567.

24 Wijshoff, H. The dynamics of the piezo inkjet printhead operation. *Phys. Rep.* **2010**, *491*, 77–177.

25 Fromm, J. E. Numerical calculation of the fluid dynamics of drop-on-demand jets. *IBM J. Res. Dev.* **1984**, *28*, 322–333.

26 Sumaiya, S.; Kardel, K.; El Shahat, A. Organic solar cell by inkjet printing—an overview. *Technologies* **2017**, *5*, 53.

27 Reis, N.; Ainsley, C.; Derby, B. Ink-jet delivery of particle suspensions by piezoelectric droplet ejectors. *J. Appl. Phys.* **2005**, *97*, 094903.

28 Stow, C. D.; Hadfield, M. G. An experimental investigation of fluid-flow resulting from the impact of a water drop with an unyielding dry surface. *Proc. R. Soc. Lond. A* **1981**, *373*, 419–441.

29 Li, J.; Rossignol, F.; Macdonald, J. Inkjet printing for biosensor fabrication: Combining chemistry and technology for advanced manufacturing. *Lab Chip* **2015**, *15*, 2538–2558.

30 Corzo, D.; Almasabi, K.; Bihar, E.; Macphee, S.; Rosas-Villalva, D.; Gasparini, N.; Inal, S.; Baran, D. Digital inkjet printing of high-efficiency large-area nonfullerene organic solar cells. *Adv. Mater. Technol.* **2019**, *4*, 1900040.

31 Soltman, D.; Subramanian, V. Inkjet-printed line morphologies and temperature control of the coffee ring effect. *Langmuir* **2008**, *24*, 2224–2231.

32 Cherian, D.; Mitra, K. Y.; Hartwig, M.; Malinowski, P. E.; Baumann, R. R. Fabrication of organic photo detectors using inkjet technology and its comparison to conventional deposition processes. *IEEE Sens. J.* **2018**, *18*, 94–105.

33 Du, Z. H.; Zhou, H.; Yu, X. H.; Han, Y. C. Controlling the polarity and viscosity of small molecule ink to suppress the contact line receding and coffee ring effect during inkjet printing. *Colloids Surf., A* **2020**, *602*, 125111.

34 Al-Milaji, K. N.; Secondo, R. R.; Ng, T. N.; Kinsey, N.; Zhao, H. Interfacial self-assembly of colloidal nanoparticles in dual-droplet inkjet printing. *Adv. Mater. Interfaces* **2018**, *5*, 1701561.

35 Kuang, M.; Wang, L.; Song, Y. Controllable printing droplets for high-resolution patterns. *Adv. Mater.* **2014**, *26*, 6950–6958.

36 Matavž, A.; Frunză, R.C.; Drnovšek, A.; Bobnar, V.; Malič, B. Inkjet printing of uniform dielectric oxide structures from sol-gel inks by adjusting the solvent composition. *J. Mater. Chem. C* **2016**, *4*, 5634–5641.

37 Jung, S.; Sou, A.; Banger, K.; Ko, D. H.; Chow, P. C. Y.; McNeill, C. R.; Sirringhaus, H. All-inkjet-printed, all-air-processed solar cells. *Adv. Energy Mater.* **2014**, *4*, 1400432.

38 Lim, J. A.; Lee, W. H.; Lee, H. S.; Lee, J. H.; Park, Y. D.; Cho, K. Self-organization of ink-jet-printed triisopropylsilylethynyl pentacene *via* evaporation-induced flows in a drying droplet. *Adv. Funct. Mater.* **2008**, *18*, 229–234.

39 Teichler, A.; Perelaer, J.; Schubert, U. S. Inkjet printing of organic electronics—comparison of deposition techniques and state-of-the-art developments. *J. Mater. Chem. C* **2013**, *1*, 1910–1925.

40 Sempels, W.; De Dier, R.; Mizuno, H.; Hofkens, J.; Vermant, J. Auto-production of biosurfactants reverses the coffee ring effect in a bacterial system. *Nat. Commun.* **2013**, *4*, 1757.

41 Marin, V.; Holder, E.; Wienk, M. M.; Tekin, E.; Kozodaev, D.; Schubert, U. S. Ink-jet printing of electron donor/acceptor blends: towards bulk heterojunction solar cells. *Macromol. Rapid Commun.* **2005**, *26*, 319–324.

42 Hoth, C.N.; Choulis, S. A.; Schilinsky, P.; Brabec, C. J. High photovoltaic performance of inkjet printed polymer:fullerene blends. *Adv. Mater.* **2007**, *19*, 3973–3978.

43 Eggenhuisen, T. M.; Galagan, Y.; Biezemans, A. F. K. V.; Slaats, T. M. W. L.; Voorthuijzen, W. P.; Kommeren, S.; Shanmugam, S.;

Teunissen, J. P.; Hadipour, A.; Verhees, W. J. H.; Veenstra, S. C.; Coenen, M. J. J.; Gilot, J.; Andriessen, R.; Groen, W.A. High efficiency, fully inkjet printed organic solar cells with freedom of design. *J. Mater. Chem. A* **2015**, *3*, 7255–7262.

44 Corzo, D.; Bihar, E.; Alexandre, E. B.; Rosas-Villalva, D.; Baran, D. Ink engineering of transport layers for 9.5% efficient all-printed semitransparent nonfullerene solar cells. *Adv. Funct. Mater.* **2020**, *31*, 2005763.

45 Jeong, J. A.; Lee, J.; Kim, H.; Kim, H. K.; Na, S. I. Ink-jet printed transparent electrode using nano-size indium tin oxide particles for organic photovoltaics. *Sol. Energy Mater. Sol. Cells* **2010**, *94*, 1840–1844.

46 Choi, K. H.; Jeong, J. A.; Kim, H. K. Dependence of electrical, optical, and structural properties on the thickness of IZTO thin films grown by linear facing target sputtering for organic solar cells. *Sol. Energy Mater. Sol. Cells* **2010**, *94*, 1822–1830.

47 Chang, Y. M.; Wang, L.; Su, W. F. Polymer solar cells with poly(3,4-ethylenedioxythiophene) as transparent anode. *Org. Electron.* **2008**, *9*, 968–973.

48 Na, S. I.; Park, D. W.; Kim, S. S.; Yang, S. Y.; Lee, K.; Lee, M. H. ITO-free flexible polymer solar cells with ink-jet-printed Ag grids. *Semicond. Sci. Technol.* **2012**, *27*, 125002.

49 Maisch, P.; Tam, K.C.; Lucera, L.; Egelhaaf, H. J.; Scheiber, H.; Maier, E.; Brabec, C.J. Inkjet printed silver nanowire percolation networks as electrodes for highly efficient semitransparent organic solar cells. *Org. Electron.* **2016**, *38*, 139–143.

50 Kim, J.; Na, S. I.; Kim, H. K. Inkjet printing of transparent InZnSnO conducting electrodes from nano-particle ink for printable organic photovoltaics. *Sol. Energy Mater. Sol. Cells* **2012**, *98*, 424–432.

51 Galagan, Y.; Coenen, E. W. C.; Sabik, S.; Gorter, H. H.; Barink, M.; Veenstra, S. C.; Kroon, J. M.; Andriessen, R.; Blom, P. W. M. Evaluation of ink-jet printed current collecting grids and busbars for ITO-free organic solar cells. *Sol. Energy Mater. Sol. Cells* **2012**, *104*, 32–38.

52 Lee, I.; Kim, G. W.; Yang, M.; Kim, T. S. Simultaneously enhancing the cohesion and electrical conductivity of PEDOT:PSS conductive polymer films using DMSO additives. *ACS Appl. Mater. Interfaces* **2016**, *8*, 302–310.

53 Kim, J.Y.; Jung, J.H.; Lee, D.E.; Joo, J. Enhancement of electrical conductivity of poly(3,4-ethylenedioxythiophene)/poly(4-styrenesulfonate) by a change of solvents. *Synth. Met.* **2002**, *126*, 311.

54 Yamaguchi, H.; Aizawa, K.; Chonan, Y.; Komiyama, T.; Aoyama, T.; Sakai, E.; Qiu, J.; Sato, N. Highly flexible and conductive glycerol-doped PEDOT:PSS films prepared under an electric field. *J. Electron. Mater.* **2018**, *47*, 3370–3375.

55 Khasim, S.; Pasha, A.; Roy, A.S.; Parveen, A.; Badi, N. Effect of secondary doping using sorbitol on structure and transport properties of PEDOT-PSS thin films. *J. Electron. Mater.* **2017**, *46*, 4439–4447.

56 Kishi, N.; Kondo, Y.; Kunieda, H.; Hibi, S.; Sawada, Y. Enhancement of thermoelectric properties of PEDOT:PSS thin films by addition of anionic surfactants. *J. Mater. Sci. Mater. Electron.* **2018**, *29*, 4030–4034.

57 Yeon, C.; Kim, G.; J; Yun, S. J. Highly conductive PEDOT:PSS treated by sodium dodecyl sulfate for stretchable fabric heaters. *RSC Adv.* **2017**, *7*, 5888–5897.

58 Lee, J. H.; Jeong, Y. R.; Lee, G.; Jin, S. W.; Lee, Y. H.; Hong, S. Y.; Park, H.; Kim, J. W.; Lee, S. S.; Ha, J. S. Highly conductive, stretchable, and transparent PEDOT:PSS electrodes fabricated with triblock copolymer additives and acid treatment. *ACS Appl. Mater. Interfaces* **2018**, *10*, 28027–28035.

59 Xia, Y.; Sun, K.; Ouyang, J. Solution-processed metallic conducting polymer films as transparent electrode of optoelectronic devices. *Adv. Mater.* **2012**, *24*, 2436–2440.

60 Hau, S. K.; Yip, H. L.; Zou, J.; Jen, A. K. Y. Indium tin oxide-free semi-transparent inverted polymer solar cells using conducting polymer as both bottom and top electrodes. *Org. Electron.* **2009**, *10*, 1401–1407.

61 Zhou, Y.; Cheun, H.; Choi, S.; Potscavage, W. J.; Fuentes-Hernandez, C.; Kippelen, B. Indium tin oxide-free and metal-free semitransparent organic solar cells. *Appl. Phys. Lett.* **2010**, *97*, 153304.

62 Galagan, Y.; Zimmermann, B.; Coenen, E. W. C.; Jørgensen, M.; Tanenbaum, D. M.; Krebs, F. C.; Gorter, H.; Sabik, S.; Slooff, L. H.; Veenstra, S. C.; Kroon, J. M.; Andriessen, R. Current collecting grids for ITO-free solar cells. *Adv. Energy Mater.* **2012**, *2*, 103–110.

63 Neophytou, M.; Hermerschmidt, F.; Savva, A.; Georgiou, E.; Choulis, S.A. Highly efficient indium tin oxide-free organic photovoltaics using inkjet-printed silver nanoparticle current collecting grids. *Appl. Phys. Lett.* **2012**, *101*, 193302.

64 Neophytou, M.; Georgiou, E.; Fyrillas, M. M.; Choulis, S. A. Two step sintering process and metal grid design optimization for highly efficient ITO free organic photovoltaics. *Sol. Energy Mater. Sol. Cells* **2014**, *122*, 1–7.

65 Kim, Y. H.; Sachse, C.; Machala, M. L.; May, C.; Müller-Meskamp, L.; Leo, K. Highly conductive PEDOT:PSS electrode with optimized solvent and thermal post-treatment for ITO-free organic solar cells. *Adv. Funct. Mater.* **2011**, *21*, 1076–1081.

66 Huang, Y. C.; Hsu, F. H.; Cha, H. C.; Chuang, C. M.; Tsao, C. S.; Chen, C. Y. High-performance ITO-free spray-processed polymer solar cells with incorporating ink-jet printed grid. *Org. Electron.* **2013**, *14*, 2809–2817.

67 Zhang, Z. L.; Si, T. T.; Liu, J. Controllable assembly of a hierarchical multiscale architecture based on silver nanoparticle grids/nanowires for flexible organic solar cells. *Nanotechnology* **2018**, *29*, 11.

68 Georgiou, E.; Choulis, S. A.; Hermerschmidt, F.; Pozov, S. M.; Burgues-Ceballos, I.; Christodoulou, C.; Schider, G.; Kreissl, S.; Ward, R.; List-Kratochvil, E. J. W.; Boeffel, C. Printed copper nanoparticle metal grids for cost-effective ITO-free solution processed solar cells. *Sol. RRL* **2018**, *2*, 1700192.

69 Pan, W.; Han, Y.; Wang, Z.; Gong, C.; Guo, J.; Lin, J.; Luo, Q.; Yang, S.; Ma, C. Q. An efficiency of 14.29% and 13.08% for 1 cm^2 and 4 cm^2 flexible organic solar cells enabled by sol-gel ZnO and ZnO nanoparticle bilayer electron transporting layers. *J. Mater. Chem. A* **2021**, *9*, 16889–16897.

70 Guo, J. B.; Han, Y. F.; Xu, Z. H.; Zha, W. S.; Fang, J.; Luo, Q.; Liu, L. Q.; Ma, C. Q. Monodispersed ZnO nanoink and ultra-smooth large-area ZnO films for high performance and stable organic solar cells. *Flex. Print. Electron.* **2022**, *7*, 025013.

71 Singh, A.; Gupta, S. K.; Garg, A. Inverted polymer bulk heterojunction solar cells with ink-jet printed electron transport and active layers. *Org. Electron.* **2016**, *35*, 118–127.

72 Sacramento, A.; Ramirez-Como, M.; Balderrama, V. S.; Garduno, S. I.; Estrada, M.; Marsal, L. F. Inverted polymer solar cells using inkjet printed ZnO as electron transport layer: characterization and degradation study. *IEEE J. Electron Devices Soc.* **2020**, *8*, 413–420.

73 Kommeren, S.; Coenen, M. J. J.; Eggenhuisen, T. M.; Slaats, T. W. L.; Gorter, H.; Groen, P. Combining solvents and surfactants for inkjet printing PEDOT:PSS on P3HT/PCBM in organic solar cells. *Org. Electron.* **2018**, *61*, 282–288.

74 Singh, A.; Gupta, S. K.; Garg, A. Inkjet printing of NiO films and integration as hole transporting layers in polymer solar cells. *Sci. Rep.* **2017**, *7*, 1775.

75 Jiang, Y.; Dong, X.; Sun, L.; Liu, T.; Qin, F.; Xie, C.; Jiang, P.; Hu, L.; Lu, X.; Zhou, X.; Meng, W.; Li, N.; Brabec, C. J.; Zhou, Y. An

alcohol-dispersed conducting polymer complex for fully printable organic solar cells with improved stability. *Nat. Energy* **2022**, *7*, 352–359.

76 Lamont, C. A.; Eggenhuisen, T. M.; Coenen, M. J. J.; Slaats, T. W. L.; Andriessen, R.; Groen, P. Tuning the viscosity of halogen free bulk heterojunction inks for inkjet printed organic solar cells. *Org. Electron.* **2015**, *17*, 107–114.

77 Aernouts, T.; Aleksandrov, T.; Girotto, C.; Genoe, J.; Poortmans, J. Polymer based organic solar cells using ink-jet printed active layers. *Appl. Phys. Lett.* **2008**, *92*, 033306.

78 Hoth, C. N.; Schilinsky, P.; Choulis, S. A.; Brabec, C. J. Printing highly efficient organic solar cells. *Nano Lett.* **2008**, *8*, 2806–2813.

79 Teichler, A.; Eckardt, R.; Hoeppener, S.; Friebe, C.; Perelaer, J.; Senes, A.; Morana, M.; Brabec, C. J.; Schubert, U. S. Combinatorial screening of polymer:fullerene blends for organic solar cells by inkjet printing. *Adv. Energy Mater.* **2011**, *1*, 105–114.

80 Eom, S. H.; Park, H.; Mujawar, S. H.; Yoon, S. C.; Kim, S. S.; Na, S. I.; Kang, S. J.; Khim, D.; Kim, D. Y.; Lee, S. H. High efficiency polymer solar cells *via* sequential inkjet-printing of PEDOT:PSS and P3HT:PCBM inks with additives. *Org. Electron.* **2010**, *11*, 1516–1522.

81 Hoth, C. N.; Choulis, S. A.; Schilinsky, P.; Brabec, C. J. On the effect of poly(3-hexylthiophene) regioregularity on inkjet printed organic solar cells. *J. Mater. Chem.* **2009**, *19*, 5398.

82 Ganesan, S.; Gollu, S. R.; Alam khan, J.; Kushwaha, A.; Gupta, D. Inkjet printing of zinc oxide and P3HT:ICBA in ambient conditions for inverted bulk heterojunction solar cells. *Opt. Mater.* **2019**, *94*, 430–435.

83 Eggenhuisen, T. M.; Galagan, Y.; Coenen, E. W. C.; Voorthuijzen, W. P.; Slaats, M. W. L.; Kommeren, S. A.; Shanmuganam, S.; Coenen, M. J. J.; Andriessen, R.; Groen, W. A. Digital fabrication of organic solar cells by inkjet printing using non-halogenated solvents. *Sol. Energy Mater. Sol. Cells* **2015**, *134*, 364–372.

84 Perkhun, P.; Köntges, W.; Pourcin, F.; Esteoulle, D.; Barulina, E.; Yoshimoto, N.; Pierron, P.; Margeat, O.; Videlot-Ackermann, C.; Bharwal, A. K.; Duché, D.; Herrero, C. R.; Gonzales, C.; Guerrero, A.; Bisquert, J.; Schröder, R. R.; Pfannmöller, M.; Ben Dkhil, S.; Simon, J. J.; Ackermann, J. High-efficiency digital inkjet-printed non-fullerene polymer blends using non-halogenated solvents. *Adv. Energy Sustain. Res.* **2021**, *2*, 2000086.

85 Lan, S.; Zhong, J.; Wang, X. Impact of inkjet printing parameters on the morphology and device performance of organic photovoltaics. *J. Phys. D: Appl. Phys.* **2021**, *54*, 465105.

86 Wang, Y.; Luo, Q.; Wu, N.; Wang, Q.; Zhu, H.; Chen, L.; Li, Y.Q.; Luo, L.; Ma, C. Q. Solution-processed MoO$_3$:PEDOT:PSS hybrid hole transporting layer for inverted polymer solar cells. *ACS Appl. Mater. Interfaces* **2015**, *7*, 7170–7179.

87 Ji, G.; Wang, Y.; Luo, Q.; Han, K.; Xie, M.; Zhang, L.; Wu, N.; Lin, J.; Xiao, S.; Li, Y.Q.; Luo, L.Q.; Ma, C.Q. Fully coated semitransparent organic solar cells with a doctor-blade-coated composite anode buffer layer of phosphomolybdic acid and PEDOT:PSS and a spray-coated silver nanowire top electrode. *ACS Appl. Mater. Interfaces* **2018**, *10*, 943–954.

88 Li, D.; Lai, W. Y.; Zhang, Y. Z.; Huang, W. Printable transparent conductive films for flexible electronics. *Adv. Mater.* **2018**, *30*, 1704738.

89 Hermerschmidt, F.; Choulis, S. A.; List-Kratochvil, E. J. W. Implementing inkjet-printed transparent conductive electrodes in solution-processed organic electronics. *Adv. Mater. Technol.* **2019**, *4*, 1800474.

90 Galagan, Y.; Shanmugam, S.; Teunissen, J. P.; Eggenhuisen, T. M.; Biezemans, A. F. K. V.; Van Gijseghem, T.; Groen, W. A.; Andriessen, R. Solution processing of back electrodes for

organic solar cells with inverted architecture. *Sol. Energy Mater. Sol. Cells* **2014**, *130*, 163–169.

91 Georgiou, E.; Savva, A.; Neophytou, M.; Hermerschmidt, F.; Demosthenous, T.; Choulis, S. A. Evaporation-free inverted organic photovoltaics using a mixture of silver nanoparticle ink formulations for solution-processed top electrodes. *Appl. Phys. Lett.* **2014**, *105*, 233901.

92 Lu, H.; Lin, J.; Wu, N.; Nie, S.; Luo, Q.; Ma, C. Q.; Cui, Z. Inkjet printed silver nanowire network as top electrode for semi-transparent organic photovoltaic devices. *Appl. Phys. Lett.* **2015**, *106*, 093302.

93 Finn, D. J.; Lotya, M.; Coleman, J. N. Inkjet printing of silver nanowire networks. *ACS Appl. Mater. Interfaces* **2015**, *7*, 9254–9261.

94 Park, E. K.; Kim, J. H.; Lee, D. H.; Kim, K. S.; Kal, J. H.; Hahn, J. S.; Kim, Y. S. All ink-jet printed P3HT:PCBM organic solar cells on ITO-coated glass substrate. *J. Nanosci. Nanotechnol.* **2015**, *15*, 8790–8796.

95 Maisch, P.; Tam, K. C.; Schilinsky, P.; Egelhaaf, H. J.; Brabec, C. J. Shy organic photovoltaics: digitally printed organic solar modules with hidden interconnects. *Sol. RRL* **2018**, *2*, 1800005.

96 Mitra, K. Y.; Alalawe, A.; Voigt, S.; Boeffel, C.; Baumann, R. R. Manufacturing of all inkjet-printed organic photovoltaic cell arrays and evaluating their suitability for flexible electronics. *Micromachines* **2018**, *9*, 642.

97 Bihar, E.; Corzo, D.; Hidalgo, T. C.; Rosas-Villalva, D.; Salama, K. N.; Inal, S.; Baran, D. Fully inkjet-printed, ultrathin and conformable organic photovoltaics as power source based on cross-linked PEDOT:PSS electrodes. *Adv. Mater. Technol.* **2020**, *5*, 2000226.

98 Patil, B. R.; Shanmugam, S.; Teunissen, J. P.; Galagan, Y. All-solution processed organic solar cells with top illumination. *Org. Electron.* **2015**, *21*, 40–46.

99 Wei, Z.; Chen, H.; Yan, K.; Yang, S. Inkjet printing and instant chemical transformation of a CH$_3$NH$_3$PbI$_3$/nanocarbon electrode and interface for planar perovskite solar cells. *Angew. Chem. Int. Ed.* **2014**, *53*, 13239–13243.

100 Li, S. G.; Jiang, K. J.; Su, M. J.; Cui, X. P.; Huang, J. H.; Zhang, Q. Q.; Zhou, X. Q.; Yang, L. M.; Song, Y. L. Inkjet printing of CH$_3$NH$_3$PbI$_3$ on a mesoscopic TiO$_2$ film for highly efficient perovskite solar cells. *J. Mater. Chem. A* **2015**, *3*, 9092–9097.

101 Chalkias, D. A.; Mourtzikou, A.; Katsagounos, G.; Karavioti, A.; Kalarakis, A. N.; Stathatos, E. Suppression of coffee-ring effect in air-processed inkjet-printed perovskite layer toward the fabrication of efficient large-sized all-printed photovoltaics: a perovskite precursor ink concentration regulation strategy. *Sol. RRL* **2022**, *6*, 2200196.

102 Gheno, A.; Huang, Y.; Bouclé, J.; Ratier, B.; Rolland, A.; Even, J.; Vedraine, S. Toward highly efficient inkjet-printed perovskite solar cells fully processed under ambient conditions and at low temperature. *Sol. RRL* **2018**, *2*, 1800191.

103 Zhang, L. H.; Chen, S.; Wang, X. Z.; Wang, D.; Li, Y.; Ai, Q.; Sun, X. Y.; Chen, J. B.; Li, Y.; Jiang, X. Z.; Yang, S. H.; Xu, B. M. Ambient inkjet-printed high-efficiency perovskite solar cells: manipulating the spreading and crystallization behaviors of picoliter perovskite droplets. *Sol. RRL* **2021**, *5*, 2100106.

104 Hashmi, S. G.; Martineau, D.; Li, X.; Ozkan, M.; Tiihonen, A.; Dar, M. I.; Sarikka, T.; Zakeeruddin, S. M.; Paltakari, J.; Lund, P. D.; Grätzel, M. Air processed inkjet infiltrated carbon based printed perovskite solar cells with high stability and reproducibility. *Adv. Mater. Technol.* **2017**, *2*, 1600183.

105 Pathak, C. S.; Paramasivam, G.; Mathies, F.; Hirselandt, K.; Schroder, V.; Maus, O.; Dagar, J.; Klimm, C.; Unger, E.; Visoly-Fisher, I. PTB7 as an ink-additive for spin-coated versus inkjet-printed perovskite solar cells. *ACS Appl. Energy Mater.* **2022**, *5*, 4085–4095.

106 Li, Z.; Li, P.; Chen, G.; Cheng, Y.; Pi, X.; Yu, X.; Yang, D.; Han, L.; Zhang, Y.; Song, Y. Ink engineering of inkjet printing perovskite. *ACS Appl. Mater. Interfaces* **2020**, *12*, 39082−39091.

107 Wilk, B.; Öz, S.; Radicchi, E.; Ünlü, F.; Ahmad, T.; Herman, A. P.; Nunzi, F.; Mathur, S.; Kudrawiec, R.; Wojciechowski, K. Green solvent-based perovskite precursor development for ink-jet printed flexible solar cells. *ACS Sustain. Chem. Eng* **2021**, *9*, 3920−3930.

108 Liang, C.; Li, P.; Gu, H.; Zhang, Y.; Li, F.; Song, Y.; Shao, G.; Mathews, N.; Xing, G. One-step inkjet printed perovskite in air for efficient light harvesting. *Sol. RRL* **2018**, *2*, 1700217.

109 Mathies, F.; Abzieher, T.; Hochstuhl, A.; Glaser, K.; Colsmann, A.; Paetzold, U.W.; Hernandez-Sosa, G.; Lemmer, U.; Quintillaa, A. Multipass inkjet printed planar methylammonium lead iodide perovskite solar cells. *J. Mater. Chem. A* **2016**, *4*, 19207−19213.

110 Huckaba, A. J.; Lee, Y.; Xia, R.; Paek, S.; Bassetto, V. C.; Oveisi, E.; Lesch, A.; Kinge, S.; Dyson, P. J.; Girault, H.; Nazeeruddin, M. K. Inkjet-printed mesoporous TiO$_2$ and perovskite layers for high efficiency perovskite solar cells. *Energy Technol.* **2019**, *7*, 317−324.

111 Schackmar, F.; Eggers, H.; Frericks, M.; Richards, B. S.; Lemmer, U.; Hernandez-Sosa, G.; Paetzold, U. W. Perovskite solar cells with all-inkjet-printed absorber and charge transport layers. *Adv. Mater. Technol.* **2021**, *6*, 2000271.

112 Schlisske, S.; Mathies, F.; Busko, D.; Strobel, N.; Rodlmeier, T.; Richards, B. S.; Lemmer, U.; Paetzold, U. W.; Hernandez-Sosa, G.; Klampaftis, E. Design and color flexibility for inkjet-printed perovskite photovoltaics. *ACS Appl. Energy Mater.* **2019**, *2*, 764−769.

113 Hou, Y.; Xie, C.; Radmilovic, V. V.; Puscher, B.; Wu, M.; Heumuller, T.; Karl, A.; Li, N.; Tang, X.; Meng, W.; Chen, S.; Osvet, A.; Guldi, D.; Spiecker, E.; Radmilovic, V. R.; Brabec, C. J. Assembling mesoscale-structured organic interfaces in perovskite photovoltaics. *Adv. Mater.* **2019**, *31*, 1806516.

114 Xie, C.; Heumuller, T.; Gruber, W.; Tang, X.; Classen, A.; Schuldes, I.; Bidwell, M.; Spath, A.; Fink, R. H.; Unruh, T.; McCulloch, I.; Li, N.; Brabec, C. J. Overcoming efficiency and stability limits in water-processing nanoparticular organic photovoltaics by minimizing microstructure defects. *Nat. Commun.* **2018**, *9*, 5335.

115 Manger, F.; Marlow, P.; Fischer, K.; Nöller, M.; Sprau, C.; Colsmann, A. Organic solar cells: electrostatic stabilization of organic semiconductor nanoparticle dispersions by electrical doping. *Adv. Funct. Mater.* **2022**, *32*, 2202566.